Finite element modeling of high frequency irreversible electroporation

by

Philip Randall

B.S., Kansas State University, 2020

A THESIS

submitted in partial fulfillment of the requirements for the degree

MASTER OF SCIENCE

Mike Wiegers Department of Electrical & Computer Engineering
Carl R. Ice College of Engineering

KANSAS STATE UNIVERSITY
Manhattan, Kansas

2021

Approved by:

Major Professor
Dr. Punit Prakash

Copyright

Abstract

High frequency irreversible electroporation (HFIRE) is a minimally invasive, non-thermal method of soft tissue ablation that has potential to effectively treat tumors and atrial fibrillation without the severe muscular contractions that occur with monophasic pulses. The technology is relatively new, and further research is needed to understand the relationship between energy delivery parameters and effects on tissue. The objective of this study was to contribute to this understanding by using finite element method (FEM) computational models of HFIRE to determine how specific electroporation waveform parameters affect ablation patterns in tissue and validating these results against experimental measurements. The effects of heterogeneous structures on electroporation profiles were also investigated with simulations. HFIRE experiments were conducted in potato tissue, an established benchtop model for electroporation studies, with a custom generator to create rapid and easily scannable lesions using varying waveform parameters. The varied waveform parameters were voltage (1000 – 2000 V), inter-pulse delay time (2 – 10 μs), pulse width (1 – 5 μs), and pulse number (25 – 75). Following experiments, a flatbed scanner was used to acquire images of the visibly discolored tissue, which has been previously shown to be indicative of the ablation pattern. The experimentally observed ablation zones were then compared to model-predictions by using image processing techniques to assess the differences in area and shape. An electric field damage threshold was assigned to each given set of waveform parameters based on which value had the best fit to the model predictions. The thresholds were in the range of 200-500 V/cm for all experiments, which is in agreement with current literature. The validated computational model was then adapted to employ properties of liver tissue, and a basic blood vessel and tumor model were incorporated to analyze the effects on the electric field inside the tumor and vessel wall. The data was presented as a dose volume histogram, and the blood vessel was found to decrease the electric field inside of the tumor as the distance between them was decreased. This decrease was approximately 100 V/cm for electric field values in the tumor that were already on the verge of being below the threshold for cell death in liver tissue. Future research could build on this study by providing more empirical conductivity and lesion data for specific tissue types.

Table of Contents

List of Figures

List of Tables

Acknowledgements

I would like to thank Dominic Hogan, Corbin Reagan, Jeff Chininis, and the staff at RBC Medical for their collaboration on this project and providing the specialized equipment necessary for experimentation. I would also like to thank Dr. Dwight Day and Dr. Charles Carlson for providing feedback on this thesis to help improve the content and writing. Finally, I would like to thank Dr. Punit Prakash for sharing his expertise and mentoring me through the process of authoring a thesis.

Chapter 1 – Background

I. Introduction

In 2020, there were approximately 42,810 cases of liver and intrahepatic bile duct cancers occurring in both men and women in the United States [1]. Of these cases, only 18% survived beyond the first five years. Liver cancer presents itself as a particularly dismal diagnosis since it is often close to critical structures such as major blood vessels, and therefore poses a high resection risk. When these tumors are deemed unresectable, minimally-invasive treatments such as thermal ablation can offer a promising alternative for some patients. However, many of the bile ducts and blood vessels continue to be problematic due to their heat-sinking effects, which significantly mitigate the efficacy of these treatments [2]; further, thermal damage to these structures can results in complications. Thermal ablation is also frequently used as a minimally-invasive surgical treatment for atrial fibrillation in patients that have exhibited resistance to beta blockers and cardioversion therapies. If left untreated, atrial fibrillation can significantly increase the chances of stroke and heart failure over time. A rare but serious complication that can occur a short period following the inadvertent heating of the esophagus wall during thermal ablation is atrioesophageal fistula, which can result in intracerebral air emboli, cardiac arrest, or other life-threatening symptoms [3]. Other serious collateral injuries that can arise due to the non-specific nature of thermal ablation are pulmonary venous stenosis, phrenic nerve injury, and damage to coronary arteries [4]. Therapies that utilize thermal energy (radiofrequency ablation, cryoablation, laser ablation, and ultrasound ablation) as a means of treating atrial fibrillation have all been found to have some risk associated with the development of an esophageal fistula [5].

Non-thermal irreversible electroporation (NTIRE) is a technique that has recently been explored as a novel method of treating atrial fibrillation and cancer in patients that are not eligible for surgery. Cells in a localized region can be effectively ablated by applying short bursts (10 - 100) of high voltage (100 – 3000 V) and current (can reach up to 50 A) across the tissue. The main advantages of using this type of treatment as opposed to thermal ablation are tissue selectivity and minimal thermal heating [4]. The tissue specificity property of NTIRE could significantly mitigate the risk of devastating injuries to the critical structures surrounding the

heart during catheter ablation since myocardial tissue is much more susceptible to the effects of NTIRE [5]. Therefore, if the pulse parameters selected (i.e. voltage, duration) are sufficiently high to destroy the myocardium while also being below the threshold of cell death for esophageal and nerve tissue, then the treatment can be delivered to the patient without the risk of atrioesophageal fistula or phrenic nerve injury. Most cells are irreversibly damaged by high thermal doses within a narrow range of time and temperatures, while the threshold for damaging cells with electroporation varies more broadly across different tissue types [4]. The non-thermal property of NTIRE also allows for the effective ablation of liver tumors without causing damage to any nearby bile ducts [6]. Since NTIRE does not rely on thermal heating to destroy tissue, the heat sinking effects produced by blood vessels and bile ducts that typically diminish the effectiveness of thermal ablation are negligible with electroporation [7].

II. Theory of Electroporation

Electroporation is a phenomenon that was first documented in 1754 by a French physicist who observed that exposure to electric sparks caused the formation of red spots on the skin of animals and humans [8]. In 1982, Neumann et al. published one of the first paper documenting the use of microsecond high voltage pulses (8 kV/cm for 5 μs) to increase the permeability of mouse cells, which greatly improved the uptake of foreign genes by these cells [9]. This medical application of electroporation is known as gene electrotransfer, and utilizes reversible electroporation since the cells do not die in the process if the exposure to the applied electric field is sufficiently short [10]. The increase in the permeability of the cell membrane is best described as a result of the formation of many aqueous pores in the lipid bilayer, which allows molecules that were previously unable to enter or exit the cell to move freely through the barrier [11]. It is hypothesized that these pores are formed when water penetrates the cell membrane and cause the hydrophilic heads of the lipids to reorient themselves towards the stream of molecules [11]. Simulations and experiments have been able to provide good evidence of a pore formation theory to explain electropermeabilization, however it is challenging to observe pore formation electrically due to the limited resolution of optical microscopes, and the preparation methods for electron microscopy inherently affect the bilayer structure [10]. A visual representation of this theorized pore formation process can be seen in Figure 1-1. These pores can develop

spontaneously even when an external electric field is not present as the formation of aqueous pores is a stochastic process, however they are unstable and do not occur frequently enough to result in any significant changes to the equilibrium of the cell [11]. The presence of an external electric field reduces the energy required for water to penetrate the membrane, and allows for a greater number of pores to form [11].

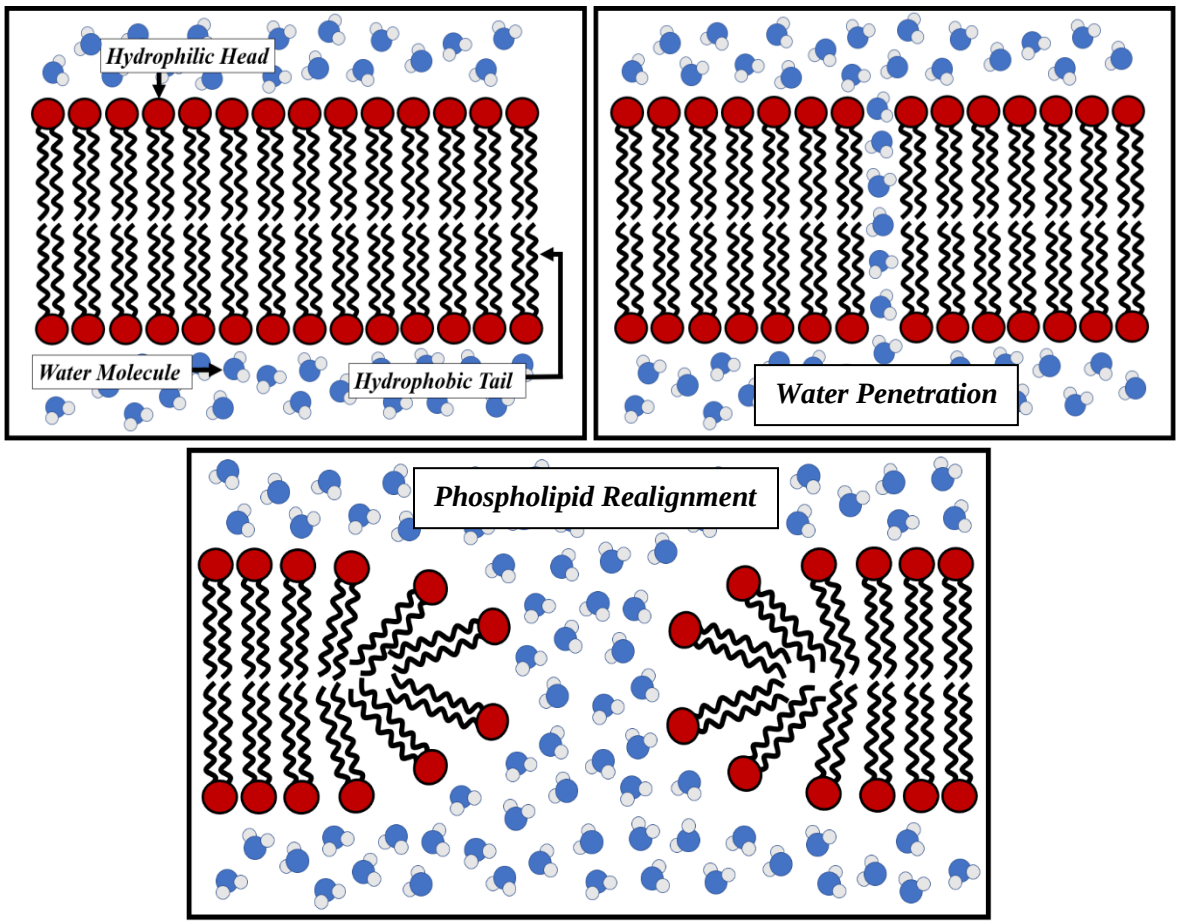

Figure 1-1: Visual representation of the theory of aqueous pore formation in the lipid bilayer. Adapted from [11]

Once the cell has been exposed to an external electric field for a few microseconds, a voltage difference begins to appear on the lipid bilayer due to the cell membrane having a much lower conductivity relative to the extracellular and intracellular mediums [12]. This voltage difference,

known as the induced transmembrane voltage (ITV), further compounds the effect of permeabilization by increasing the likelihood of pore formation and increasing the stability of the existing pores. The magnitude of the ITV is most pronounced when the membrane is perpendicular to the external electric field, and nearly non-existent when parallel (cosine relationship) [13]. Once the external electric field is removed, the ITV disappears and the pores begin to reseal in a similar stochastic manner to how they formed. The main difference between formation and resealing is the duration of the event, as formation occurs within nanoseconds to microseconds, whereas resealing can take seconds or even minutes on the membrane of a live cell [11].

As stated previously, NTIRE is in clinical use for non-thermal ablation of disease in patients that are not eligible for surgery. The main parameters that determine the efficacy of the treatment are the voltage of each pulse and the total number of pulses in the treatments. These values must be selected carefully to ensure that the resulting treatment zone is appropriate for the target disease, especially with cancer since residual disease may lead to local progression. It is common for researchers to determine an electric field threshold required to effectively ablate tissue, however this approach is incomplete since NTIRE is a function of both electric field and duration of exposure. The death of cells due to the effects of NTIRE can be more practically described on a macroscopic level using statistical models. An example of this can be seen in Figure 1-2 with a contour plot of cell death probability versus pulse voltage and total pulses.

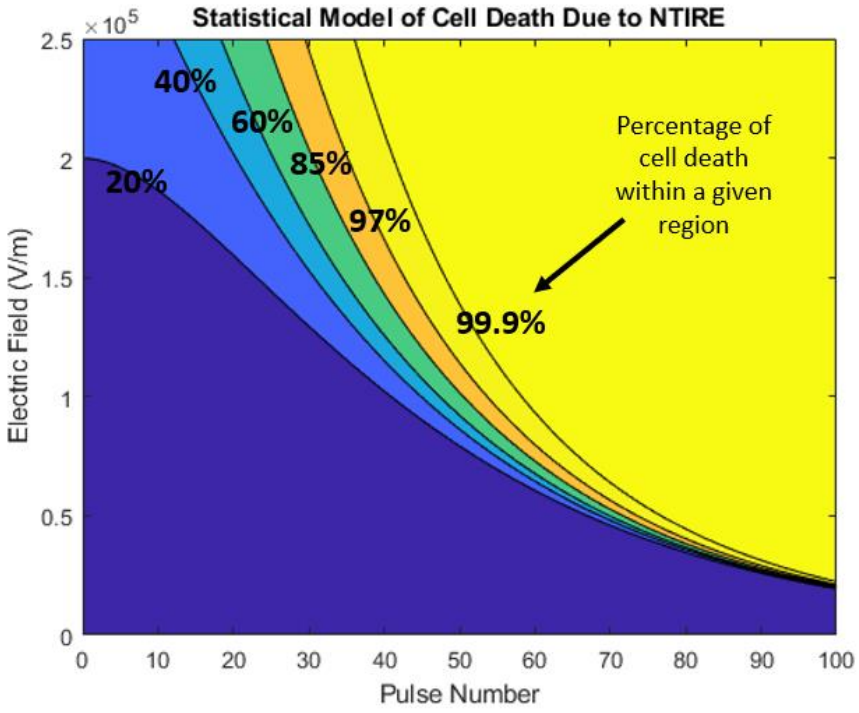

Figure 1-2: Contour plot of cell death probability with input arguments electric field strength and pulse number. The plot was generated in MATLAB using a statistical model developed by Goldberg et al., and is based on prostate tissue properties. Adapted from [14], [15]

Other parameters that are important to consider when planning a treatment are the shape of the waveform and pulse width. Traditionally, simple rectangular pulses were used to deliver the energy required to achieve an ITV in the cell membranes. This type of waveform is commonly referred to as monophasic since the pulses are all of positive amplitude. An issue that presents itself during monophasic NTIRE treatments is severe muscle contraction due to neuromuscular electrical stimulation, which must be quelled using paralytic agents otherwise the probes delivering the energy could move and miss the target zone or damage vital structures [16]. Introducing a positive and negative amplitude component (biphasic) into the waveform to cancel out the DC signal solves this issue since the contractions are primarily caused by the low frequency components contained by the monophasic waveform. These low frequency components can also produce more unpredictable lesions in heterogeneous tissue since tissue

impedance is more uniform at higher frequencies [17]. An example of typical monophasic and biphasic waveforms can be seen in Figure 1-3.

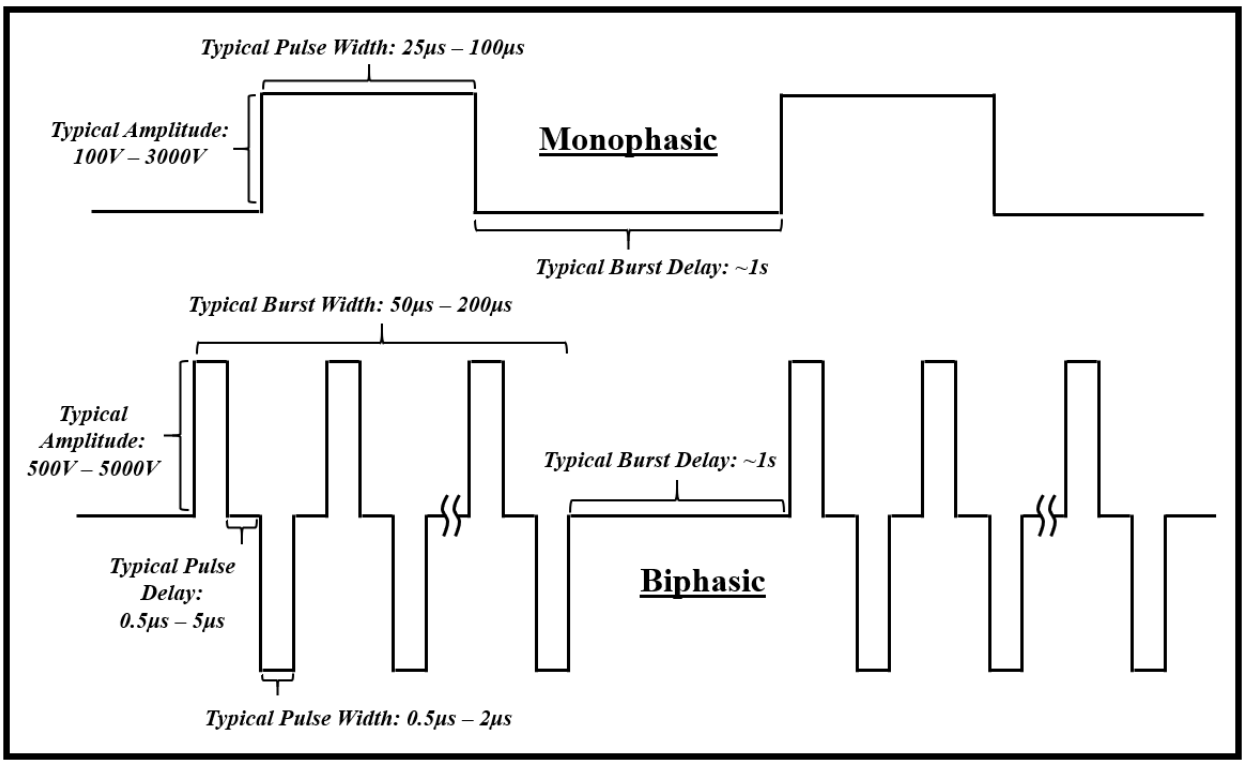

Figure 1-3: Illustration of monophasic and biphasic waveforms with their typical parameter ranges [18], [19]

The pulse width is also an important consideration since pulse widths that are too large can result in significant heating and widths that are too small can lead to decreased cell death. This decrease in cell death due to insufficient pulse width occurs because of a delay in the ITV created by the externally applied field, similar to a highpass filter response. Biphasic waveforms can also present this problem if the frequency is too high (approximately >1MHz) [16].

III. Hardware and Modeling

The hardware used to deliver the necessary energy, typically referred to as a generator, must be able to to handle the voltage, timing, and safety requirements necessary for effective

irreversible electroporation treatments. NTIRE generators typically employ high-energy capacitive charging to deliver large voltage pulses to a tissue load of variable impedance [20]. The discharging is controlled by power MOSFETs and IGBTs that are driven by FPGA logic to attain high-precision timing protocols [20]. The design and placement of the electrodes is the most critical part of the system as they are ultimately what deliver the energy to the patient. Electrode configurations can range from a single bipolar probe to an array of many electrodes (usually up to six) to completely encompass the target tissue. If the electrodes are either designed or placed improperly, several safety issues could arise such as leakage current into the patient, sparking, electrocution, or unnecessary damage to healthy tissue. Figure 1-4 shows the first FDA cleared NTIRE system used to treat patients, along with the probes designed for the unit.

Figure 1-4: The NanoKnife system and the probes designed for the unit. Obtained from a NanoKnife vendor website [21]

Finite-element analysis is a method commonly used to design electrodes for NTIRE, and to serve as a computational engine for planning of individual treatments [22]. However, inaccurate results due to incomplete modeling can lead to significant deviation in the desired outcome if the models are part of the treatment planning process. Simulating electric fields and currents may be useful for clinicians when making decisions about how to treat a patient. Generally speaking, the current literature that exists on irreversible electroporation in homogenous tissue using monophasic voltage waveforms is robust with good indication that *in silico* experiments match well with *in vivo* results [23]. Literature exploring how heterogeneous structures, such as biliary ducts, affect the electric field distribution is not as abundant, and is something this research seeks to expound upon. Another recent innovation is the use of biphasic waveforms to irreversibly electroporate tissue, also known as high-frequency irreversible electroporation (HFIRE). The ultimate objective of irreversible electroporation is to develop an optimized method of treatment planning which maximizes the destruction of target tissue while minimizing collateral damage to healthy cells. This approach would theoretically be similar to how radiation therapy is planned in the sense that a computer algorithm analyzes images of the region and determines the ideal placement of the electrodes based on the properties and location of the surrounding healthy tissue. Computerized treatment planning has greatly contributed to the precise, safe, and effective delivery of radiation therapy, and availability of similar treatment planning tools for NTIRE has potential to contribute to improved treatment outcomes [24]. The effect of changing different parameters of the waveform must also be well understood in order to deliver optimized treatment.

This study aims to contribute to the development of a computation model of HFIRE. The model developed in this study was validated against experiments in simplified, homogenous tissue (i.e. potato). Once the *in silico* models have been deemed reasonably accurate, the results will be extrapolated to a liver model by updating the tissue properties to investigate the effects of introducing heterogeneities. The results from these studies will hopefully provide more insight into the nature of how specific waveform parameters affect the lesion pattern observed in tissue, and also create a better understanding of how significantly heterogenous structures can affect these treatments.

Chapter 2 – Experimental Investigations

I. Introduction

Benchtop experiments were performed to validate the *in-silico* models. These experiments will also serve to document the effects of varying specific waveform parameters, one at a time, while holding all other settings constant. Potato tissue was chosen as the test material since tuber is inexpensive and readily available, easy to work with, and reliably produces melanin upon cellular membrane destabilization [25]. The tuber samples are quite rigid when purchased fresh, which makes it simple to section and scan each sample after energy is applied. The process by which melanin is produced in the cells after death allows for the lesion to be visible in the tissue without any additional treatment, and the pale potato tissue allows for excellent contrast with the dark lesion making image post-processing highly accurate. All of these factors allow for this process to have a high repeatability factor, allowing for more experiments to be carried out with a greater variety of waveform parameters.

Various parameters of the HFIRE waveform have been shown to affect on the outcome of electroporation treatments, particularly voltage amplitude, frequency, and burst number [17]. Different generator designs allow for certain parameters to be adjusted within a range to provide the highest degree of control to the clinician administering the treatment, however these adjustable parameters are not very useful if the doctor does not know how the parameters affect the ablation region. Voltage is a simple method of controlling the ablation zone since a higher voltage on the electrode yields a greater electric field, resulting in a larger lethal threshold region. The waveform frequency is governed by several parameters (the shape of the waveform), which are important to consider since the electrical impedance spectrum of most human tissue is not constant and subject to change during the course of an electroporation treatment [26]. An example of a conductivity vs frequency relationship in human liver tissue can be seen in Figure 2-1. Burst number can be understood probabilistically since the likelihood that a cell will be destroyed during exposure to a large electric field increases as the strength of the field is amplified. When enough bursts are applied to the tissue, the region of dead tissue will start to plateau since NTIRE can only kill cells up to a certain critical electric field threshold [17]. An

increase in temperature can also affect the outcome of a treatment since the conductivity of tissue increases with temperature.

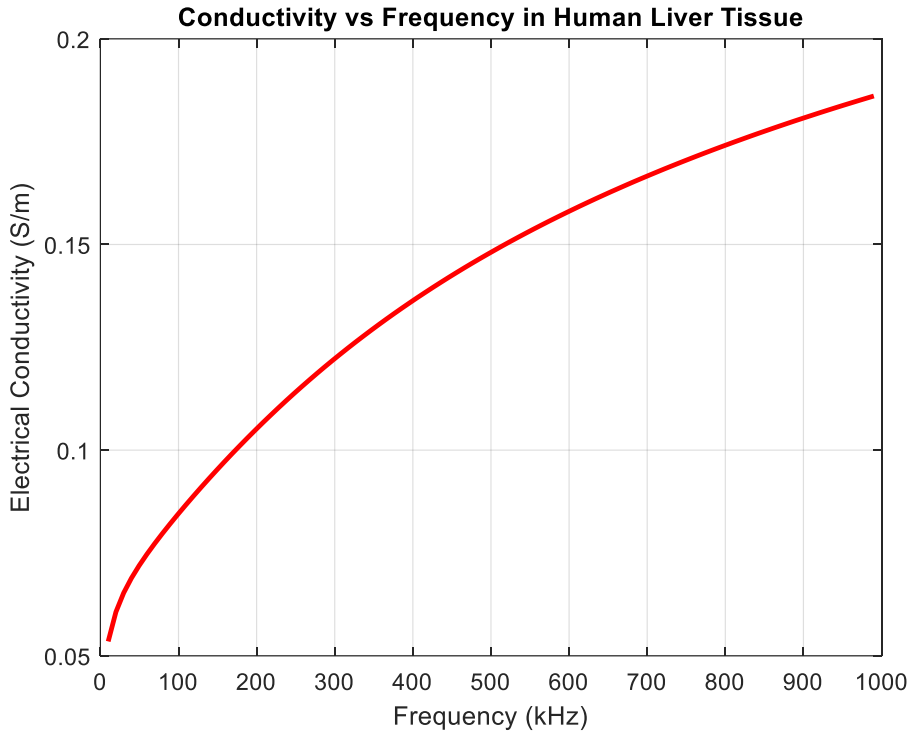

Figure 2-1: Plot of the electrical conductivity of human liver as a function of frequency. Data obtained from IT'IS Foundation tissue properties database [27].

An increase in conductivity will result in a smaller electric field yielding the same current density, which can be observed in the relationship below:

$$\mathbf{J} = \sigma\mathbf{E}$$

where **J** is current density (A/m^2), **E** is electric field (V/m), and σ is electric conductivity (S/m). After the first pulse, the main contributor to increased conductivity during the treatment is predominantly due to thermal effects [28]. It should be noted that since electroporation is a non-

thermal procedure, these temperature rises are typically very minimal, especially with HFIRE treatments (usually no more than 5°C in most cases).

II. Materials and Methods

The experiments were completed using a custom HFIRE generator prototype developed at RBC Medical Innovations in Lenexa, Kansas. The waveform output can be seen in Figure 2-2.

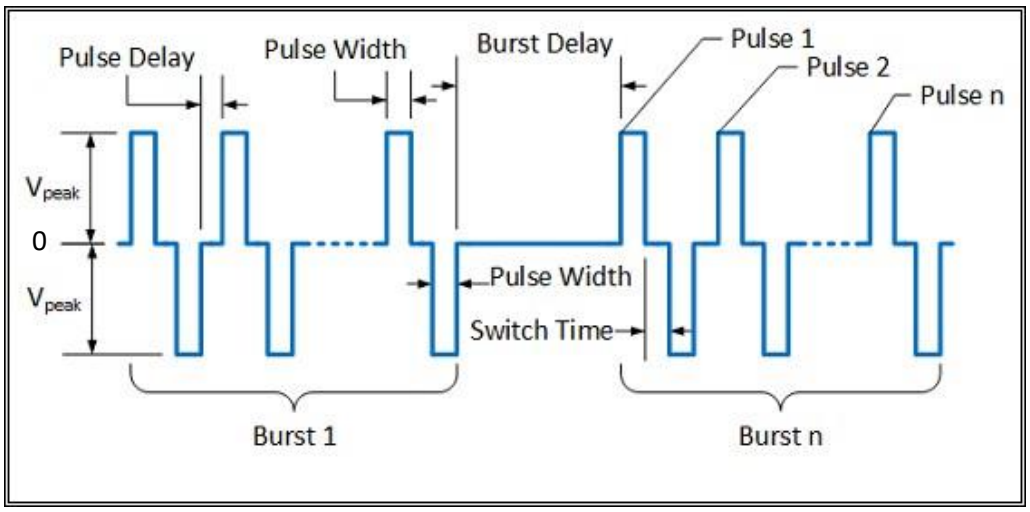

Figure 2-2: Waveform output of HFIRE generator with each adjustable setting labeled.

The settings that can be controlled are the peak voltage, pulse width, switch time, pulse delay, pulses per burst, burst delay, and burst count. Table 2-1 contains the generator settings that were used in each experiment. The parameters selected in each trial were designed to observe changes over a single setting while the others were held constant. Each experiment was repeated $n = 3$ times since biological tissues exhibit high variability, and multiple trials would improve the quality of data (in case any of the samples need to be thrown out) without increasing the work load significantly. A pair of stainless-steel tubing with an outer diameter of 2.08 mm were used to deliver the energy to the potato samples. Heat shrink was utilized to insulate the shaft of the tube with 5 mm of exposure allotted on the tip, and a sufficient exposure on the other end to allow an alligator clip to be connected from the generator. An optical temperature sensor

(Qualitrol T1C-02-PP10) was inserted equidistant between the two probes to measure the temperature change in two of the experiments. The temperature sensor was guided into the sample by using a removable needle with a flexible sheath. These three items were aligned by using a 3D printed cap placed on top of the potato to ensure that the probes were properly spaced and parallel in the sample. The spacing used between the two hollow tubes was either 15 mm or 20 mm. Each potato sample was sliced from Russet potatoes purchased from a local grocery store the same day as the experiments. The top and bottom of each potato were cut off to create flat stable surfaces, and each potato yielded about two or three samples. A high voltage differential probe and current probe (Tektronix P5210A High-Voltage Differential Probe, Pearson Current Monitor Model 110) were used to monitor the output of the generator during each procedure. The generator also has internal voltage and current monitoring that can be viewed once the energy delivery is completed. The generator is controlled by a laptop that also monitors and stores the temperature data. A visual representation of the setup can be seen in Figure 2-3.

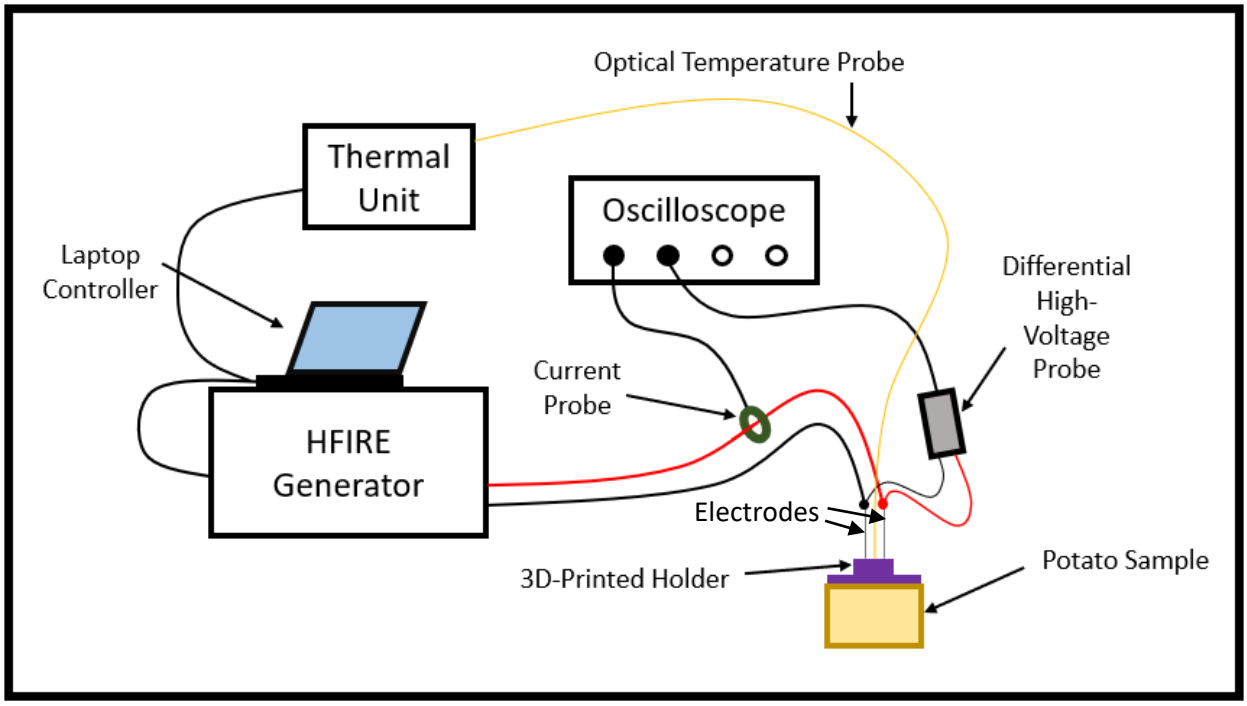

Figure 2-3: Visual representation of the setup used to electroporate potato samples.

Once the HFIRE treatment had been completed, each potato sample was stored at room temperature for 24-48 hours to allow for the lesion to develop [17]. Once the time had elapsed, the potato was sliced along the probe tracks to expose the plane of electroporated tissue with a maximal area. A flatbed scanner was used to image the samples, and the images were processed in MATLAB to determine the area of the ablated region by using an RGB analysis. A binary image was first obtained by setting all pixels with a red value less than 110 or a green value less than 60 (with a max of 256). A Gaussian blur was then applied, and then the image was eroded and dilated five times with a disk of size 12 to remove the probe tracks and any other incorrectly identified regions. Any holes in the blobs were filled, and a boundary was drawn around the lesion so that it could be visually inspected to ensure accuracy. An image with a region of known area was used to calibrate the scanner and determine the area occupied by each pixel for the given resolution of 600 DPI. The temperature probe was omitted from a majority of the experiments since the change in electrical properties between the probe and the potato tissue could potentially alter the electric field pattern. The probe was only included when temperature rise was the sole parameter being measured. The list of parameters that were used in each experiment are seen in Table 2-1. The order in which the experiments were performed was randomized to minimize any unaccounted sources of error such as probe corrosion.

Table 2-1: Generator electrical parameter variations during experiments in potato tissue

Experiment No.	Voltage (V)	Pulse Width (µs)	Switch Time (µs)	Pulse Delay (µs)	Pulses Per Burst	Burst Delay (s)	Burst Count	Electrode Dist. (mm)	Temp. Probe?
6	1500	5	2	2	50	1	90	20	No
7	1500	5	4	4	50	1	90	20	No
8	1500	5	6	6	50	1	90	20	No
9	1500	5	8	8	50	1	90	20	No
10	1500	5	10	10	50	1	90	20	No
11	1500	1	5	5	200	1	90	20	No
12	1500	2	5	5	100	1	90	20	No
13	1500	3	5	5	67	1	90	20	No
14	1500	4	5	5	50	1	90	20	No
15	1500	5	5	5	40	1	90	20	No
26	1500	2	5	5	25	1	10	15	No
27	1500	2	5	5	50	1	10	15	No
28	1500	2	5	5	75	1	10	15	No
29	1000	2	5	5	50	1	10	15	No
30	1500	2	5	5	50	1	10	15	No
31	2000	2	5	5	50	1	10	15	No
32	1500	2	5	5	50	1	10	15	Yes
33	2000	2	5	5	50	1	10	15	Yes

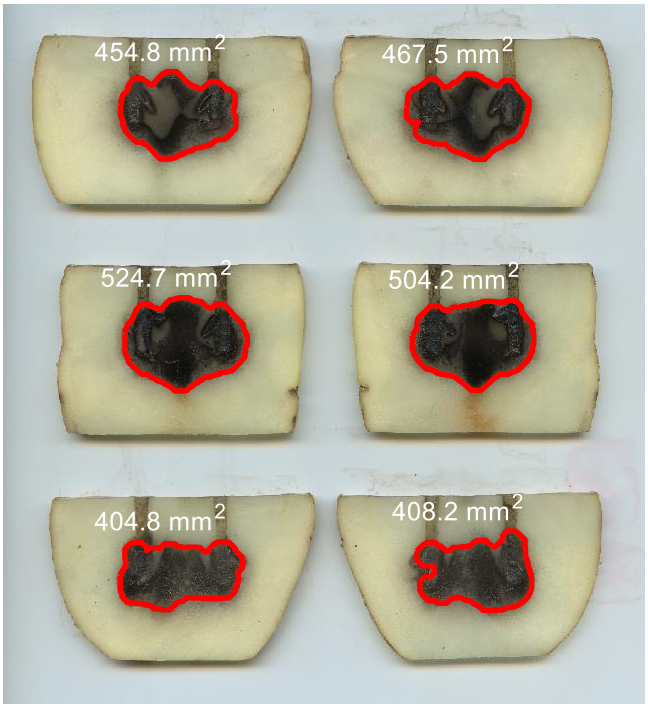

Figure 2-4: Output example from automated lesion tracing script of experiment 14

An example of the result of segmenting the lesion with automated boundary tracing script can be seen in Figure 2-4. The automated script did not work very well with experiments 26-31 since the lesions were much smaller and exhibited more discoloration in the ablated cell region. For these samples, the boundary was drawn manually in Microsoft Paint. An example of manually drawn samples can be seen in Figure 2-5, alongside the same image with automated boundaries for comparison.

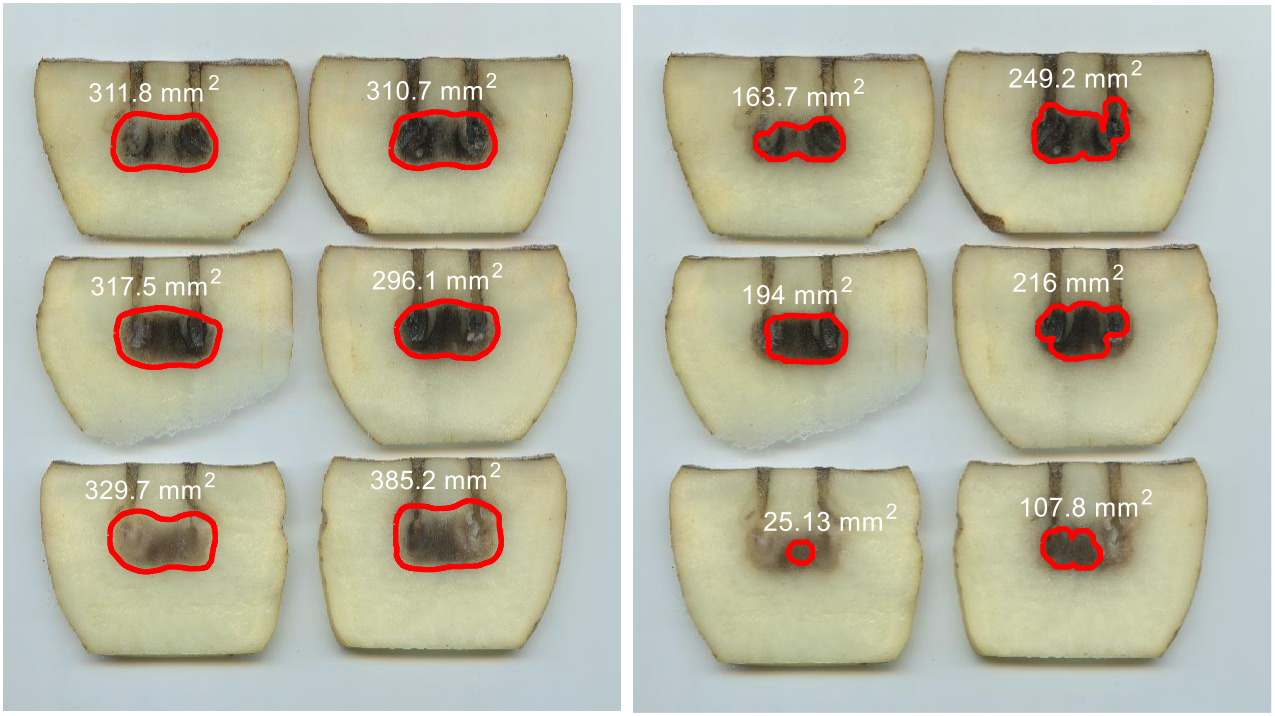

Figure 2-5: Output example from manually traced lesions processed in MATLAB of experiment 28

III. Results

Each potato sample yielded two area quantities for each half, resulting in six total values for a parameter set. These results were averaged, resulting in a single value for each experiment. The experimental results are listed in Table 2-2. Plots of the resulting averages are presented in Figure 2-7, and Figure 2-8 shows similar data for pulse delay and pulse width, except the

analysis is done with manually drawn lesion boundaries instead of the automatic segmentation. The temperature rise observed from experiments 32 and 33 can be seen in Figure 2-8.

Table 2-2: Resulting lesion areas of each potato sample. All values are area in units of mm^2. EX represents samples that were excluded from the data pool.

Experiment No.	1A	1B	2A	2B	3A	3B	Set Average	Set Std. Dev.
6	588.7	556.8	527.1	554.3	EX	EX	556.7	25.23
7	433.9	459.1	520.3	516.4	481.9	505.1	486.1	34.41
8	531.8	495.9	506.7	454.4	449.2	464.2	483.7	32.93
9	577.0	583.5	EX	EX	EX	EX	580.3	4.596
10	394.4	425.7	407.0	464.4	434.7	412.6	423.1	24.66
11	407.8	335.2	282.0	326.7	286.5	363.3	333.6	47.58
12	408.0	381.8	404.6	466.6	438.8	428.0	421.3	29.73
13	405.0	445.5	403.9	437.3	393.7	492.3	429.6	36.87
14	454.8	467.5	524.7	504.2	404.8	408.2	460.7	48.89
15	481.6	472.7	508.8	531.7	504.0	524.2	503.8	23.15
26	253.6	231.3	237.1	247.6	260.9	233.1	243.9	11.99
27	282.6	307.1	365.6	377.5	296.1	323.5	325.4	38.36
28	311.8	310.7	317.5	296.1	329.7	385.2	325.2	31.36
29	135.9	141.5	205.2	229.0	215.3	224.4	191.9	42.03
30	261.9	288.8	305.4	318.1	309.9	251.5	289.3	27.18
31	389.9	387.0	418.3	420.6	444.0	411.3	411.9	21.22

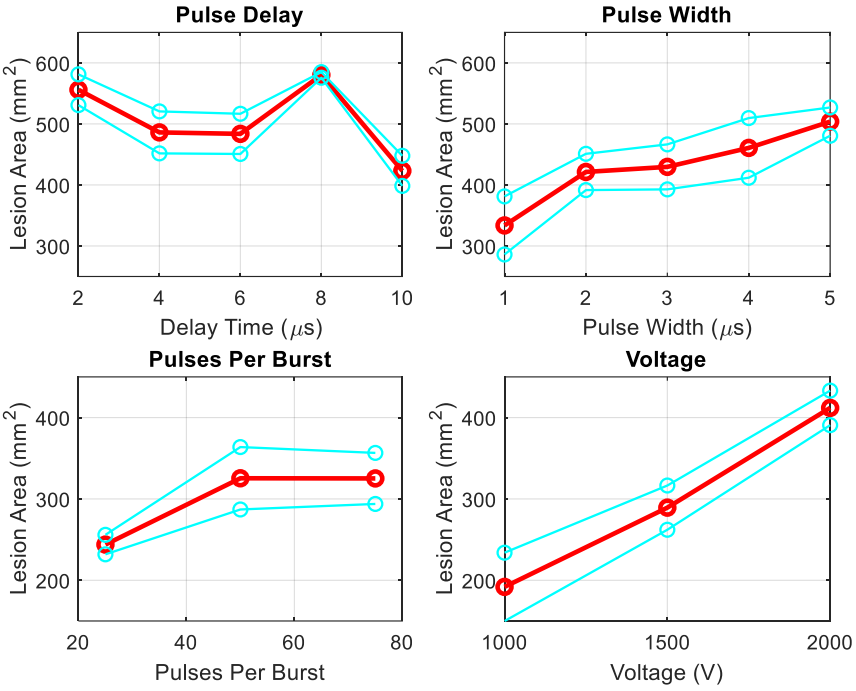

Figure 2-6: Plots of the resulting lesion areas vs the respective parameter varied in the experiment. The red line represents the average area, and the cyan is +/- one standard deviation. Note that the top two graphs use higher energy settings than the bottom two, and therefore use different y-axis scales since the lesion sizes are larger.

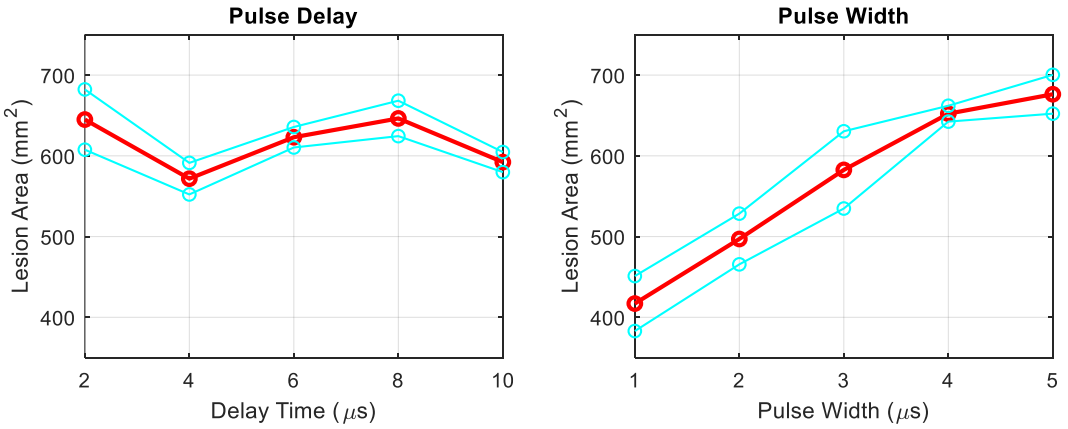

Figure 2-7: Plots of pulse delay and width with manually drawn lesion boundaries instead of automated

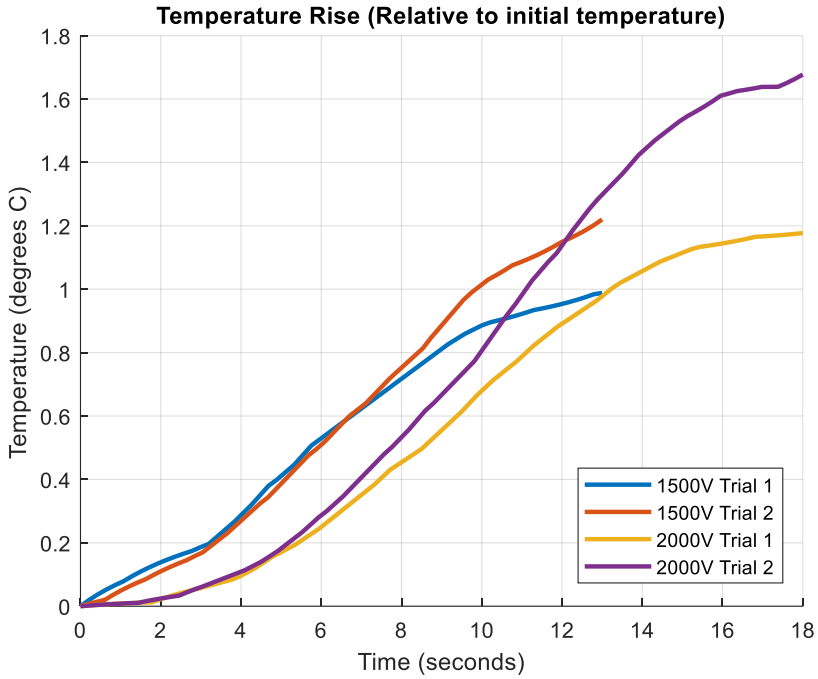

Figure 2-8: Temperature rise observed in experiments 32 and 33. Note that the increase is only around 1-2 °C at the low pulse setting

IV. Discussion

The results from each experiment agree with the data presented in existing literature. An increase in the delay/switch time from 2 µs to 10 µs resulted in a lesion decrease of 133.6 mm^2 (24% decrease), which could potentially be expected since Figure 2-1 indicates that a decrease in frequency results in decreased conductivity in tissue. However, the changes observed in delay/switch time may not be significant since this parameter did not yield any discernible trend in outputs. The waveforms used in experiment 6-10 were constructed in MATLAB and the mean frequency of each waveform was calculated. The relationship between mean frequency and delay time can be seen in Figure 2-9. The mean frequency only experiences a 5% decrease, which may not be enough to actually observe any changes in the lesion size. An increase in pulse width from 1 µs to 5 µs results in an increase in the lesion size of 170.3 mm^2 (51% increase), even with energy held constant. This was also demonstrated by Miklovic et al., and the relationship was shown to be logarithmic with a correlation coefficient of 0.995 [17]. The effect of pulses per

burst on lesion size appears to plateau after a sufficient number of pulses are applied, however more data would be needed to confirm this.

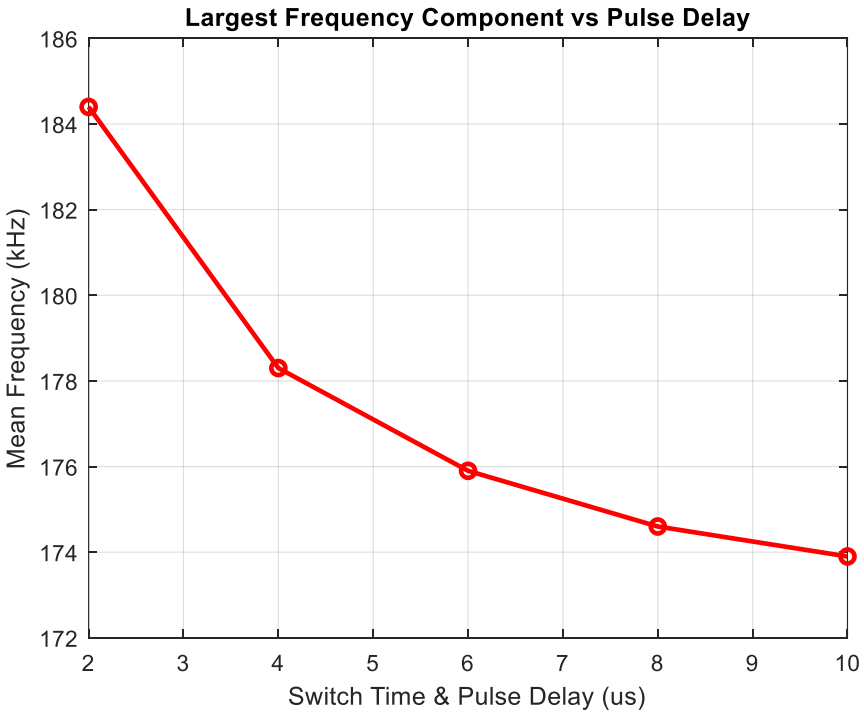

Figure 2-9: Graph of largest frequency component vs delay time in HFIRE waveform

Burst number has also been shown to increase the ablation area as more energy is applied up to a certain threshold [17]. The experiments in this study show that an increase from 25 to 75 pulses per burst yield a lesion increase of 81.2 mm^2 (33% increase). Burst number and pulse number could be understood in a similar manner since they both increase the energy delivered to the sample without changing the voltage pattern in the tissue, which would indicate that there is a certain energy dosage that can be applied that will maximize the lesion for a given pulse width and voltage setting. Voltage appears to result in a linear increase in the lesion size, which was also demonstrated in Berkenbrock et al. [29]. The experiments in this study show that an increase from 1000 V to 2000 V yields an increase in the lesion size of 220.0 mm^2 (115% increase). The temperatures in experiments 32 and 33 were only observed to rise by about 2-3

°C, which would result in a negligible increase in the electrical and thermal conductivity of the tissue.

Several experiments (not listed in Table 2-1 or Table 2-2) were performed with parameters such as pulses per burst and burst number, but had to be discarded due to technical challenges with the generator. The current iteration of the design does not support inter-pulse charging, which would allow the capacitors to recharge during the one second delay between bursts. It was discovered after performing the experiments that the given energy settings were causing the voltage to droop down to nearly half of the initial value before reaching the end of the treatment. This could have been easily addressed if the voltages and currents for each pulse were known, however the internal oscilloscope had malfunctioned during the experiments and all of the data logs were lost. A total of 15 experiments were discarded since the energy delivered to the potatoes was different for each experiment, and therefore extent of the droop for each experiment is unknown. Experiments 6-10 only varied the switch times and experiments 11-15 changed pulse width while adjusting the pulses per burst to ensure that the same amount of energy was being delivered to each sample. The droop that occurred between these experiments should be the same, and any significant change in the lesion pattern would be a result of the changing parameters. Experiments 26-31 were carried out after the error was discovered to reacquire data for voltage and pulse per burst variations. The probe separation was dropped to 15 mm to ensure that a lesion would still be visible with the lower energy settings.

Ideally, more experiments would have been performed to provide a more robust dataset, however the technology and availability of current electroporation generators make this somewhat challenging. The data that was obtained will be useful for providing a reference to ensure that the models established in the next chapter are reasonably accurate. Some issues that would have to be addressed to improve the quality of electroporation experiments are increasing the sample size, improving imaging techniques, and creating more consistent lesions. Increasing the sample size is primarily an issue of time and resources, especially if the samples were to be animal tissue instead of potatoes. More samples would help mitigate any variability that exists between samples, which is of particular concern since biological tissue is very prone to variability in properties. Automated lesion tracing would be preferred to manual since a computer will be exceptionally consistent between samples, whereas a human may not follow the

same set of rules each time. This study used a simple RGB analysis to isolate the lesions, which worked well when it was large and contrasted. Some issues began to arise when the lesions were partially discoloring for unknown reasons, which is why manual tracing was used. An example of some lesions with discoloration can be seen in Figure 2-10.

Figure 2-10: Example of discoloration in set 9 that makes it difficult to automatically process the lesion boundaries with an RGB analysis

The automated image processing script could potentially be improved by incorporating some machine learning elements to remove any misidentified data that is obviously not part of a lesion, such as the potato skin or the probe tracks. A classifier could also be developed to sort out what is healthy tissue, dark lesion tissue, discolored lesion tissue, and everything else based on a large database of expected RGB values for each category. Some research on the best method for processing the potatoes following energy delivery could also be helpful for preventing discoloration and maximizing the contrast and consistency of the lesion that develops.

Chapter 3 – Finite Element Modeling

I. Introduction

Finite element modeling could potentially be an effective method for allowing clinicians to understand how an NTIRE treatment will transpire. It is important to understand which facets of the tissue properties and delivered waveform parameters will significantly affect the simulation results and which parameters do not have a substantial impact on the predicted outcome since minimizing planning time can be critical. One feature that varies from patient to patient is the surrounding structures, which can influence the electric field pattern within the tissue and cause unforeseen distortions if not accounted for. The potatoes (tissue phantom) used in the previous chapter were generally homogenous, and variation in the lesion would be predominantly caused by uniform changes in the tissue properties or method of energy delivery. Some examples of heterogeneity that that could potentially affect treatments are the introduction of varying sizes of blood vessels, bile ducts in the liver, bones, tissue/organ boundaries, and anisotropic tissue. Tumors are often classified as unresectable because of adjacency to some critical structure that introduces heterogeneity. It is important for ablation treatments to be complete since recurrence can occur if even a small volume of viable cancer cells remain post-treatment. Recent clinical trials showed that of a pool of 169 NTIRE patients, approximately 30% experienced recurrence within 18 months, with a greater proportion occurring in patients with larger tumors [30]. Investigating the effect of heterogeneities could potentially provide insight as to what causes these recurrences.

II. Materials and Methods

A 3D finite element modeling software (COMSOL Multiphysics v5.6) was used to create all of the models in this study. The simulator was used to model the electric field patterns created by the voltage applied to the probes and the resulting electromagnetic heating from current flow. The electric field was solved using the equation:

$$\nabla \cdot (\sigma \nabla \varphi) = 0$$

where φ is the voltage (V) and σ is the electric conductivity of the material (S/m). A voltage of V_0 was applied to the exposed tip of one of the electrodes, and the other probe was set to ground. An electric insulation boundary condition was applied to the shaft of the probe (heat shrink) and all external boundaries, and can be mathematically described in the equation:

$$\frac{d\varphi}{dn} = 0$$

The heating was solved using the Pennes' bioheat equation with added Joule heating term:

$$\rho C_p \frac{\partial T}{\partial t} = \nabla \cdot (k\nabla T) + \omega_b C_b \rho_b (T_a - T) + q''' + \sigma|\mathbf{E}|^2$$

where ρ is the density of tissue (kg/m^3), Cp is the specific heat of tissue (J/kg/K), k is the thermal conductivity of tissue (W/m/K), T is temperature (K), ω_b is the blood perfusion rate (1/s), C_b is the specific heat of blood (J/kg/K), ρ_b is the density of blood (kg/m^3), Ta is arterial temperature (K), and q''' is the metabolic heat generation in tissue (W/m^3). The metabolic heating term is omitted in simulation since the magnitude of this term is typically much smaller than the other terms. The Joule heating term is averaged over the entire duration of the treatment instead of calculating the heating from each individual pulse.

The geometry of the model attempts to replicate the experimental setup used in the previous chapter. Two hollow probes are inserted parallel into a cylindrical sample with a height of 30 mm and a diameter of 30 mm. The outer and inner diameters of the probes are 2.1 mm and 1.8 mm respectively. The exposed length of the probe is 5 mm, and the separation is 15 mm. A render of the models can be seen in Figure 3-1 and 3-2. The electric conductivity of the medium is defined as a function of the electric field, which captures the increase in current caused by the microscopic pores created in the cell membranes. An example of an electric conductivity vs electric field curve can be seen in Figure 3-3, and the equation used can be seen below [31]:

$$\sigma(\mathbf{E}) = 0.03 + \frac{0.33}{1 + 10e^{\frac{65000 - \mathbf{E}}{13750}}}$$

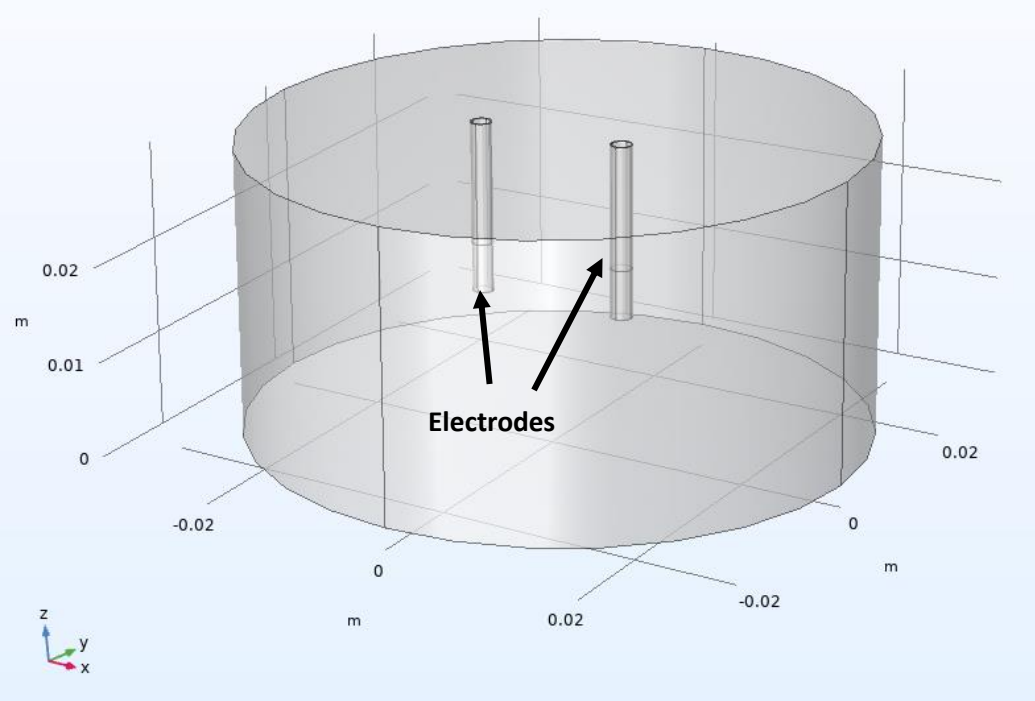

Figure 3-1: 3D geometry of the tuber model in COMSOL Multiphysics

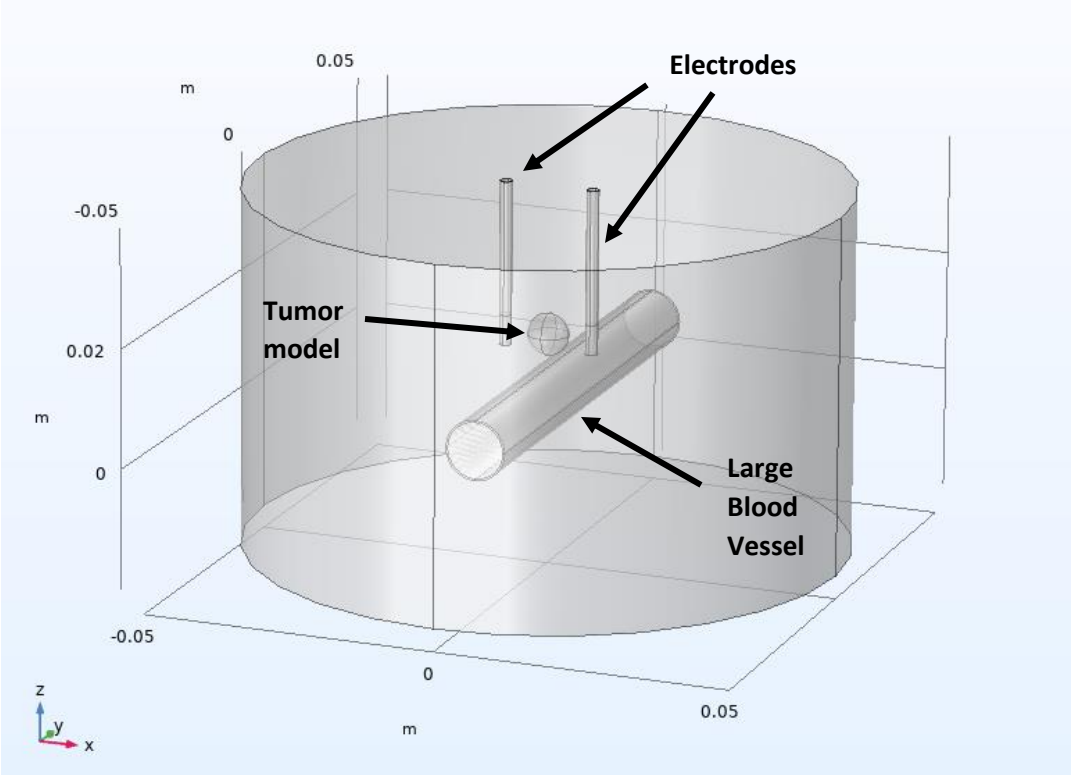

Figure 3-2: 3D geometry of the liver model in COMSOL Multiphysics

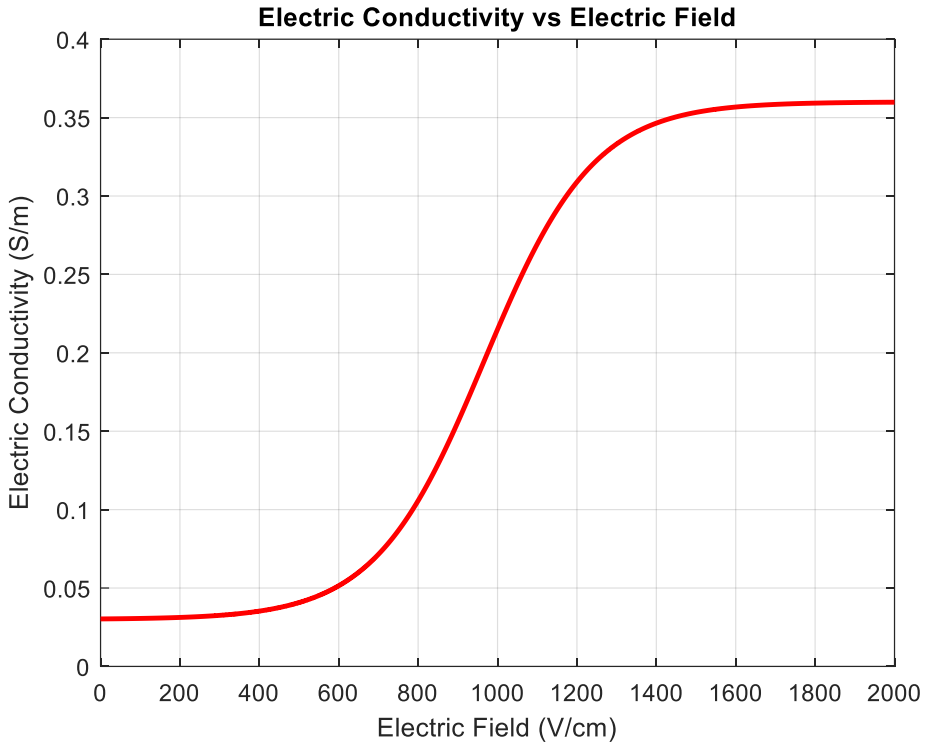

Figure 3-3: Example sigmoid curve for potato tissue developed for monopolar waveforms [31]

The mesh created to solve the model was refined until the results exhibited little perceptible change (less than 1% change in lesion area/volume). The default 'finer' setting was utilized, which generated 123175 elements with a maximum size of 3.3 mm in the potato model and 363877 elements with a maximum size of 5.5 mm in the liver model. An image of the generated mesh for both models can be seen in Figure 3-4 and Figure 3-5.

The various parameters of the waveform must be reliably accounted for in the simulation to ensure accurate results. A single deterministic death threshold value for electric field is used to describe the macroscopic lesion border that is practically observed in real-world experiments as opposed to using a statistical model. This threshold is then swept over a range of values to observe which value best fits the given set of data. The voltage amplitude can be accounted for in the simulator by simply changing the potential on the probe. The effects of frequency, pulse width, and pulse number could be incorporated by introducing changes to the conductivity curve, however more empirical data is needed to understand how these changes can be accurately modeled.

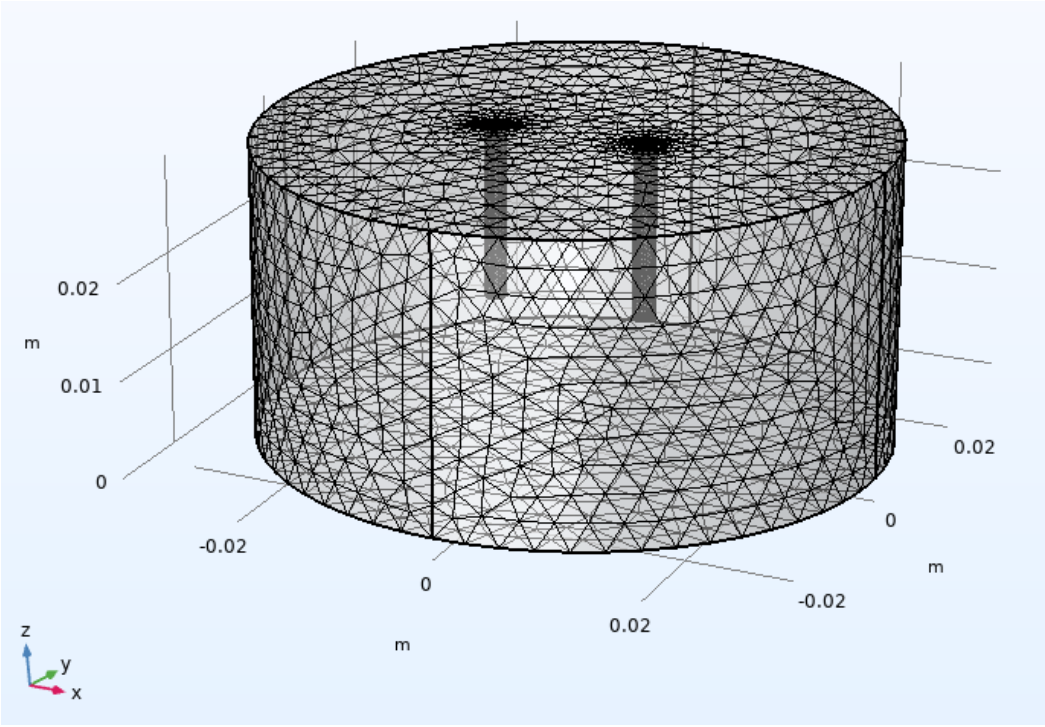

Figure 3-4: Generated mesh for tuber model

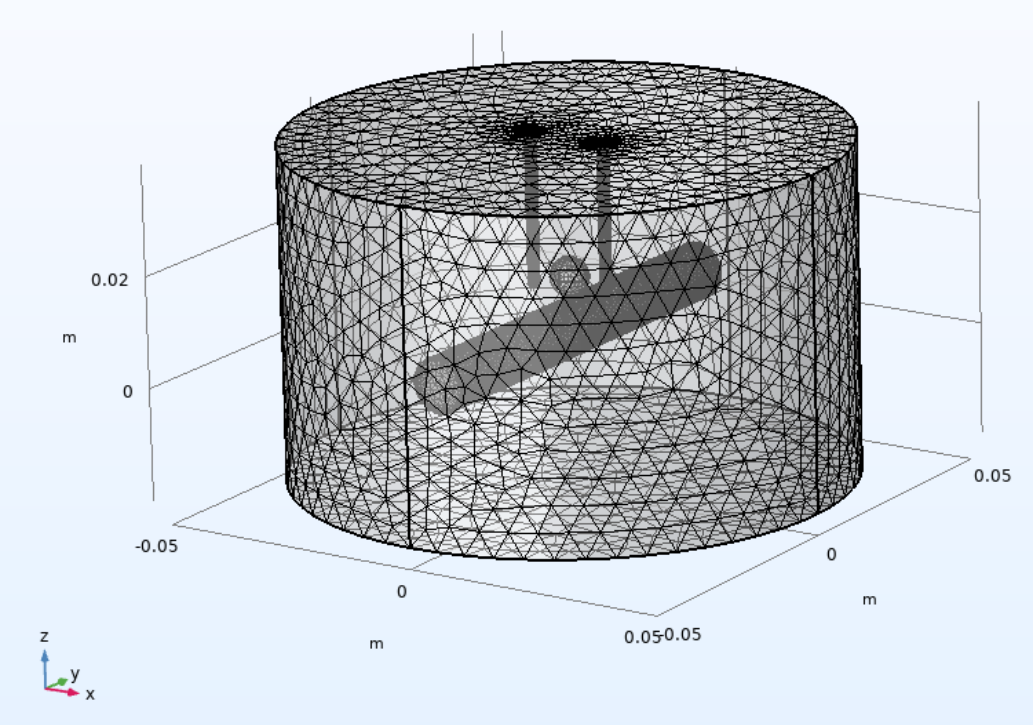

Figure 3-5: Generated mesh for heterogenous liver model

This study employed a tissue conductivity as a function of electric field, but did not account for the impact of pulse width, frequency, pulse number or burst number on conductivity. Thermal effects can be accounted for by describing the electric and thermal conductivity as a function of temperature [23]. This study omits these effects since the temperature rises are typically small within the treatment zone (less than 5°C), and is even less so with the inclusion of a perfusion model.

Two models were developed in this study: one to validate the findings from experiments conducted in potato tissue (as described in chapter 2), and another to investigate the impact of heterogeneous structures on the ablation outcome. The latter swaps out potato tissue properties for liver properties, and also includes a basic tumor model. The sample size in the tuber model is 60 mm in diameter and 30 mm in height, which is similar to that of the actual experiments. The liver model medium has a 60 mm height and a 100 mm diameter. The tuber model does not have the perfusion model since potatoes do not have any blood flow or heat production from metabolism. The electric conductivity curve parameters used for both the tuber and liver models can be seen in Table 3-1.

Table 3-1: Conductivity curve parameters used for each tissue type in COMSOL Multiphysics

Tissue	From/Start (S/m)	To/End (S/m)	Location/Center (V/cm)	Transition Zone (V/cm)	Reference
Potato	0.039	0.53	298	650	[32]
Liver	0.23	0.44	1200	350	[28]

The electric conductivity of the remaining structures in the liver model utilizes a static conductivity value since there is limited data available regarding dynamic conductivity changes in blood vessels and cancerous tissue. The conductivities used for cancerous liver tissue, blood vessel wall, and blood are 0.411, 0.232, and 0.7 S/m respectively [33],[34]. A temperature rise analysis is be performed for both the potato tissue and liver tissue without heterogeneities present. A table of the thermal properties used can be seen in Table 3-2.

Table 3-2: Thermal properties of tissues used in COMSOL Multiphysics

Tissue	Heat Capacity (J/kg*K)	Thermal Conductivity (W/m*K)	Density (kg/m^3)	Reference
Potato	3480	0.55	1070	[35],[36]
Healthy Liver	3540	0.52	1079	[27]
Cancerous Liver	3960	0.57	1040	[37]

The potato lesion data from the previous chapter and the data acquired from simulations were compared by assessing two parameters: area and shape. A range of electric field thresholds were used to calculate the resulting area within the boundary in COMSOL, and the values from experiment and simulation were compared by finding the error (difference) between the two. The shapes were compared by utilizing the Dice similarity coefficient (DSC), which is a pixel-by-pixel comparison of each lesion. The equation used to calculate the coefficient is as follows:

$$DSC = \frac{2|A \cap B|}{|A| + |B|}$$

where A and B represent the binary image data. The area data used for comparison was the averaged values from the six samples of each tuber experiment, and the DSC was calculated for each of the six lesions and then averaged across each experiment.

For the heterogenous experiments, the electric field data was acquired for multiple orientations and spacings of the blood vessel. The data is presented as a dose volume histogram for the tumor and the blood vessel wall. The tumor is 7 mm in diameter, and the vessel is 10 mm in diameter with a wall thickness of 0.5 mm.

III. Results

Figure 3-6 shows an electric field profile of a 2D cut plane parallel to the electrodes in the tuber model, similar to how the potatoes were sliced and imaged on the bench.

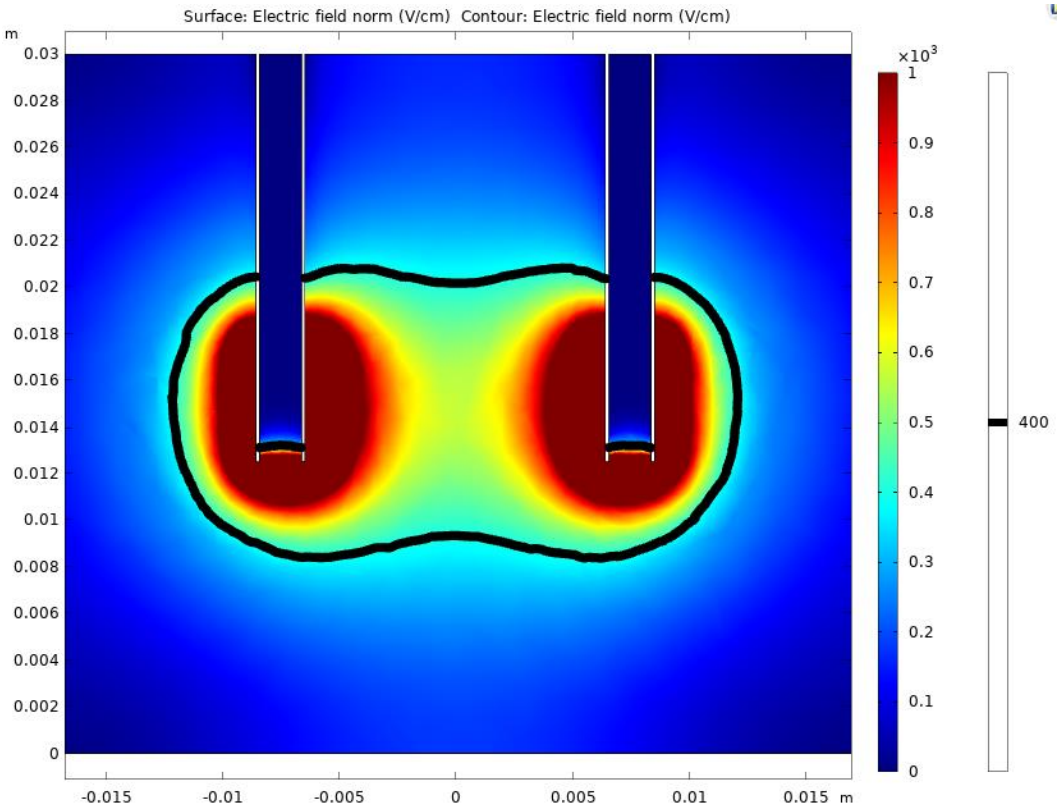

Figure 3-6: Electric field profile of the plane parallel to the two electrodes in the tuber model

The black contour line in Figure 3-4 represents the electric field threshold used for comparing the simulation profile to the experimental ablations. Figures 3-7, 3-8, 3-9, and 3-10 depict a sweep of threshold areas calculated in COMSOL and the corresponding errors when compared to the real-world experiments. Figures 3-11, 3-12, 3-13, and 3-14 depict the DSC values calculated over a range of electric field thresholds. All of the graphs were created with the data from the hand-drawn lesion boundaries. No parameters were changed in the delay/switch time, pulse width, and pulse number experiments. The voltage on the probe was changed in the simulator only for the voltage experiments to match the voltage used on the generator. Note that the method used to find the area within the contour did not include the area of the probes. This had to be determined and added manually through visual inspection since the bench experiments included the probe area within the ablation zone.

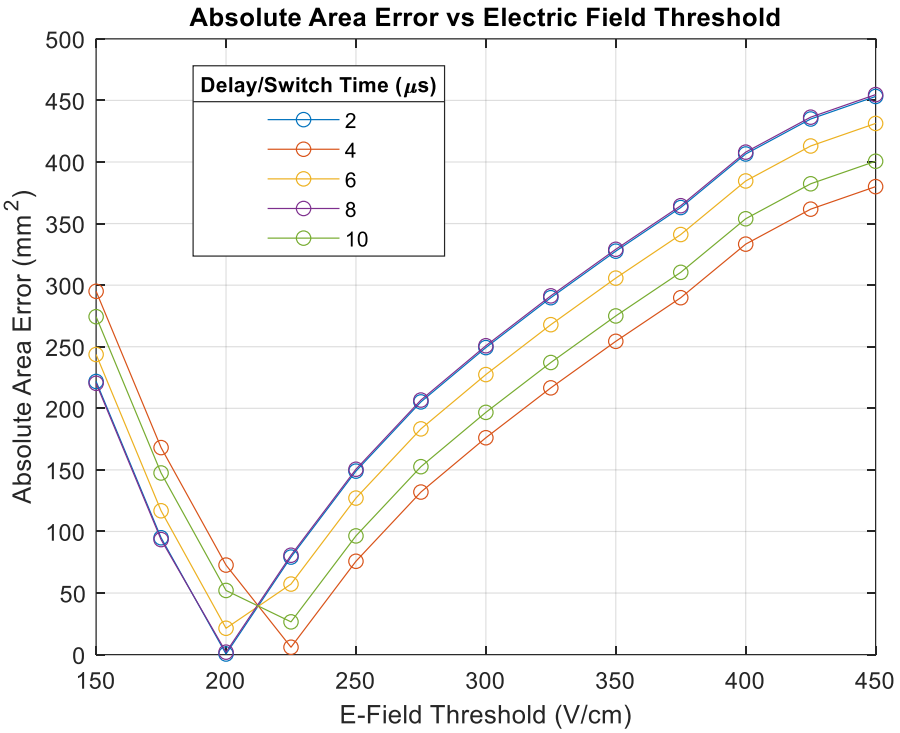

Figure 3-7: Electric field threshold value vs absolute area error of delay/switch time experiments

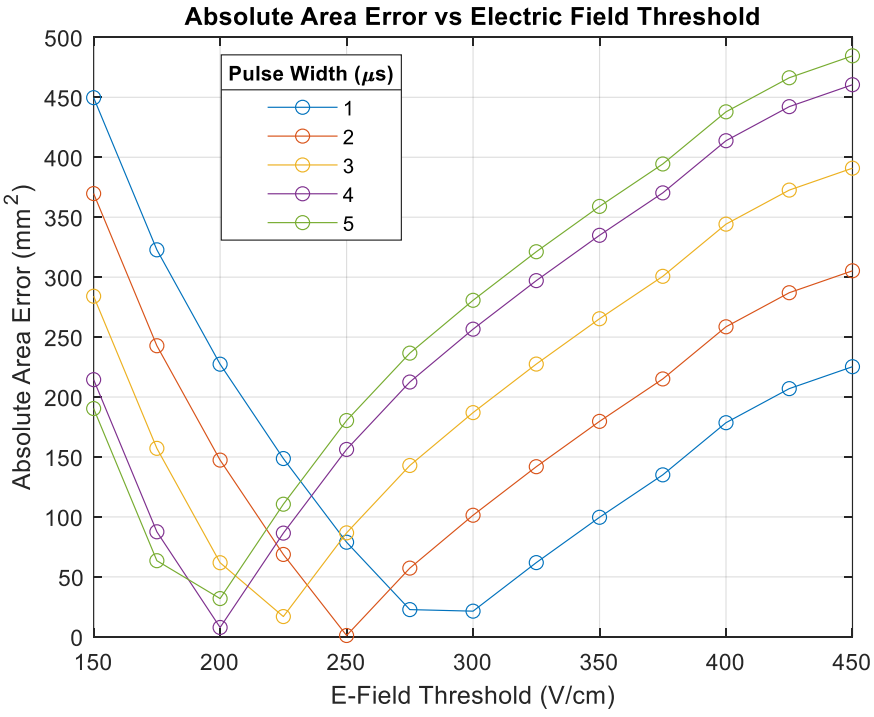

Figure 3-8: Electric field threshold value vs absolute area error of pulse width experiments

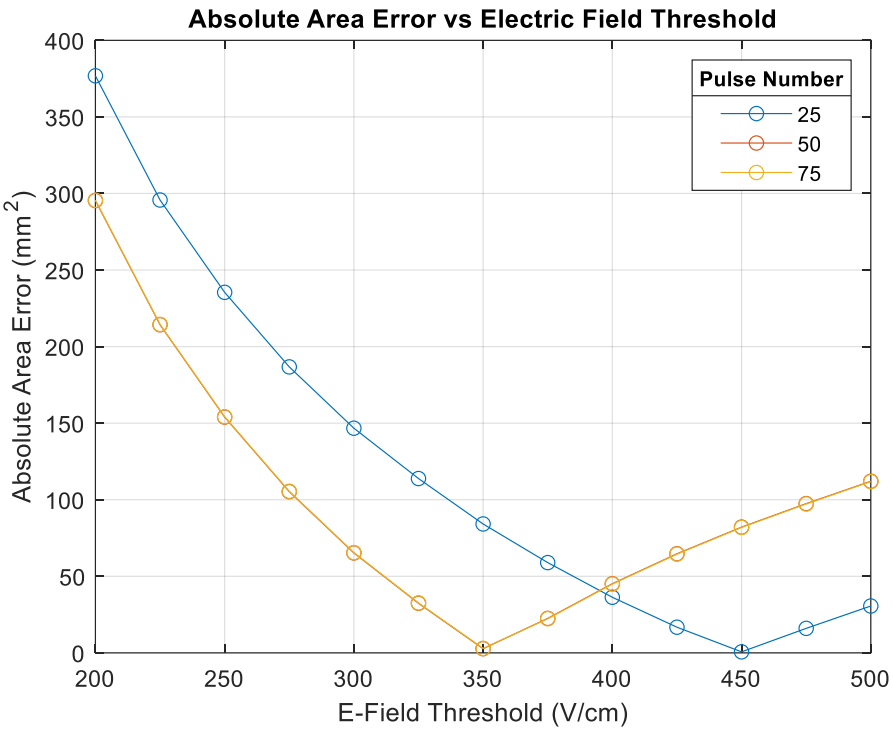

Figure 3-9: Electric field threshold value vs absolute area error of pulse number experiments

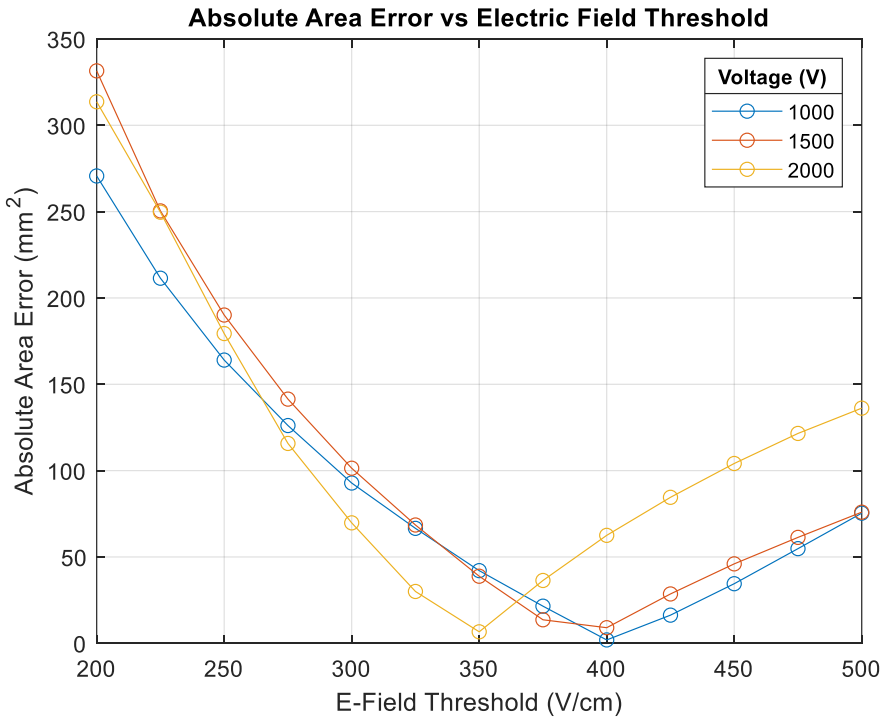

Figure 3-10: Electric field threshold value vs absolute area error of voltage experiments

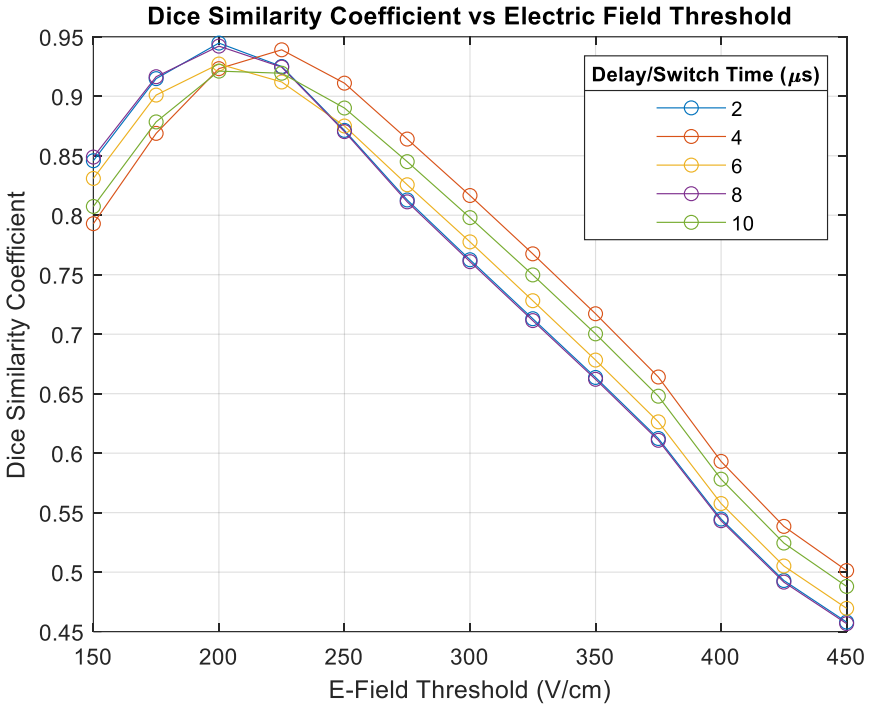

Figure 3-11: Electric field threshold value vs Dice similarity coefficient of delay/switch time experiments

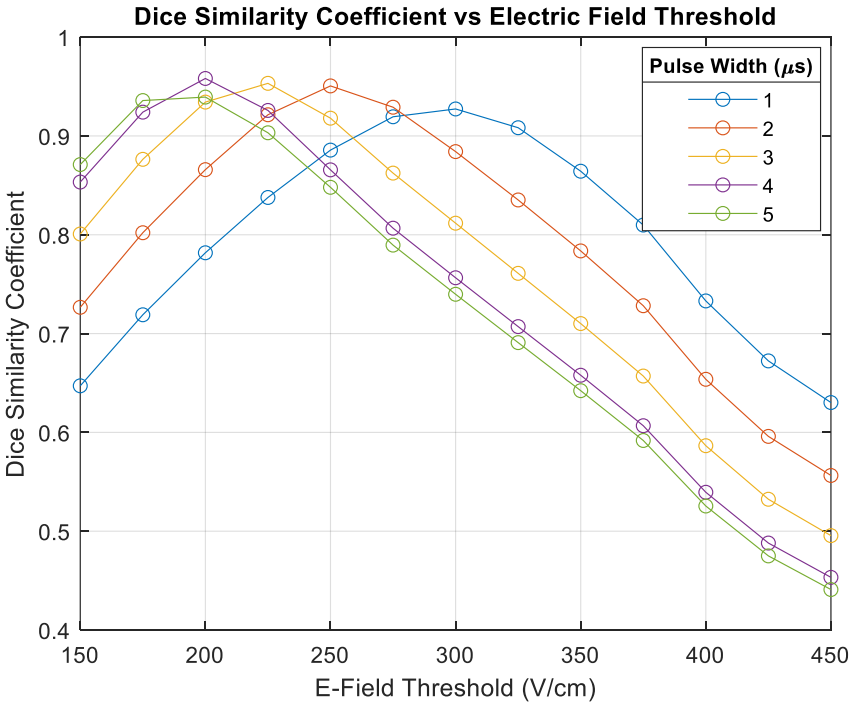

Figure 3-12: Electric field threshold value vs Dice similarity coefficient of pulse width experiments

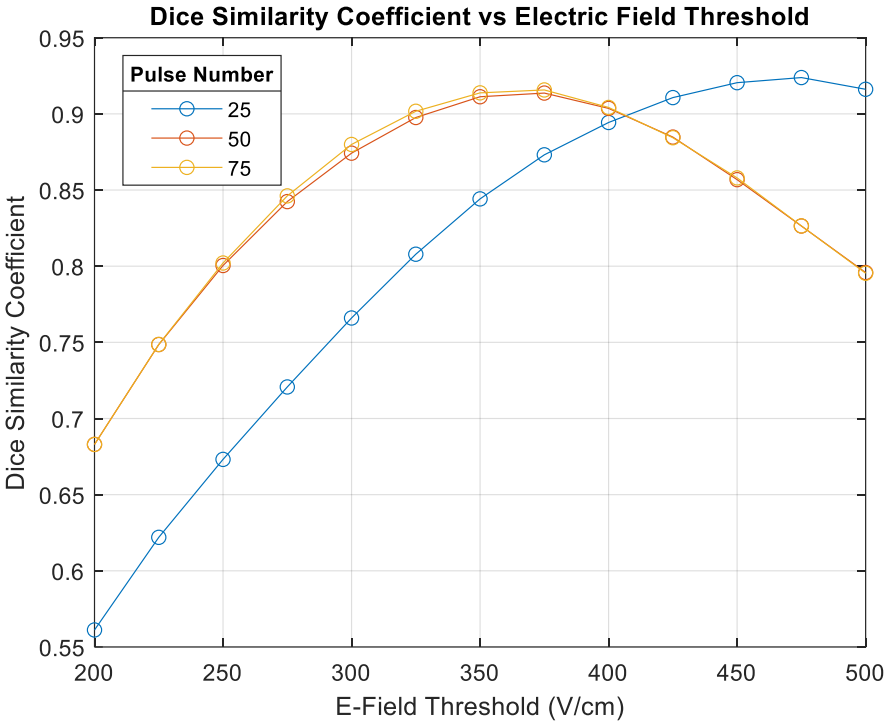

Figure 3-13: Electric field threshold value vs Dice similarity coefficient of pulse number experiments

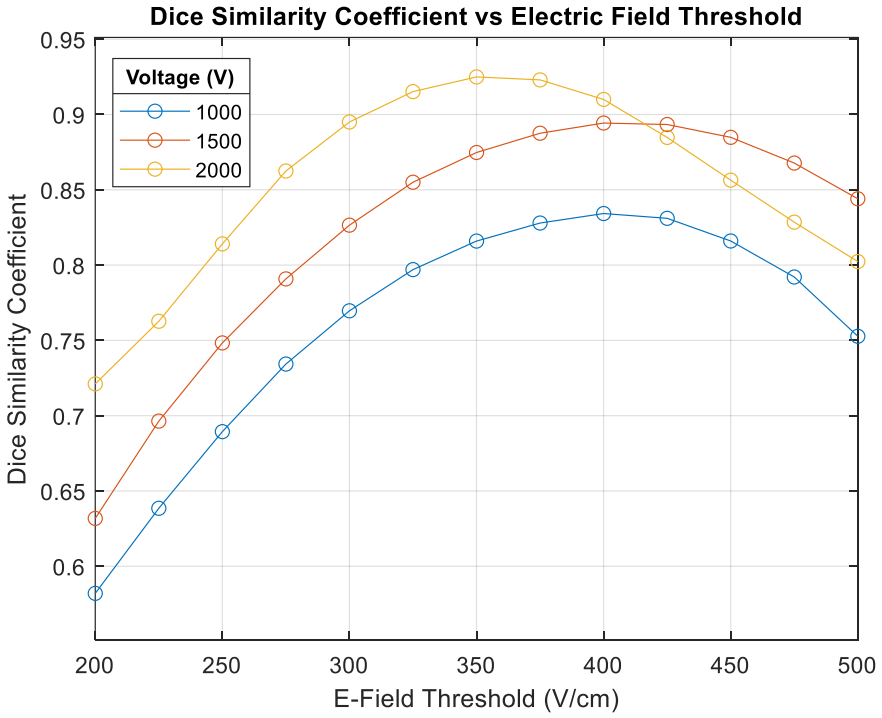

Figure 3-14: Electric field threshold value vs Dice similarity coefficient of voltage experiments

The local minima and maxima of each curve represents the electric field threshold value set in simulation that best fits the given parameters. Table 3-3 presents the threshold data that best fits each dataset, rounded to the nearest 25 V/cm interval. The temperature rise determined in simulation for voltages of 1.5 kV and 2 kV were found to be 1.1 and 1.7 °C respectively, compared to the 1-2 °C observed experimentally.

Table 3-3: Electric field thresholds (in V/cm) that best fit each experiment

	Delay/Switch Time (us)					Pulse Width (us)					Pulse Number			Voltage (kV)		
Param.	2	4	6	8	10	1	2	3	4	5	25	50	75	1	1.5	2
Area	200	225	200	200	225	300	250	225	200	200	450	350	350	400	400	350
DSC	200	225	200	200	200	300	250	225	200	200	475	375	375	400	400	350

The heterogenous model includes an electric field analysis with the blood vessel in three different orientations relative to the tumor. Figure 3-15 depicts the initial positioning of each setup. The orientations are labeled for reference in the data.

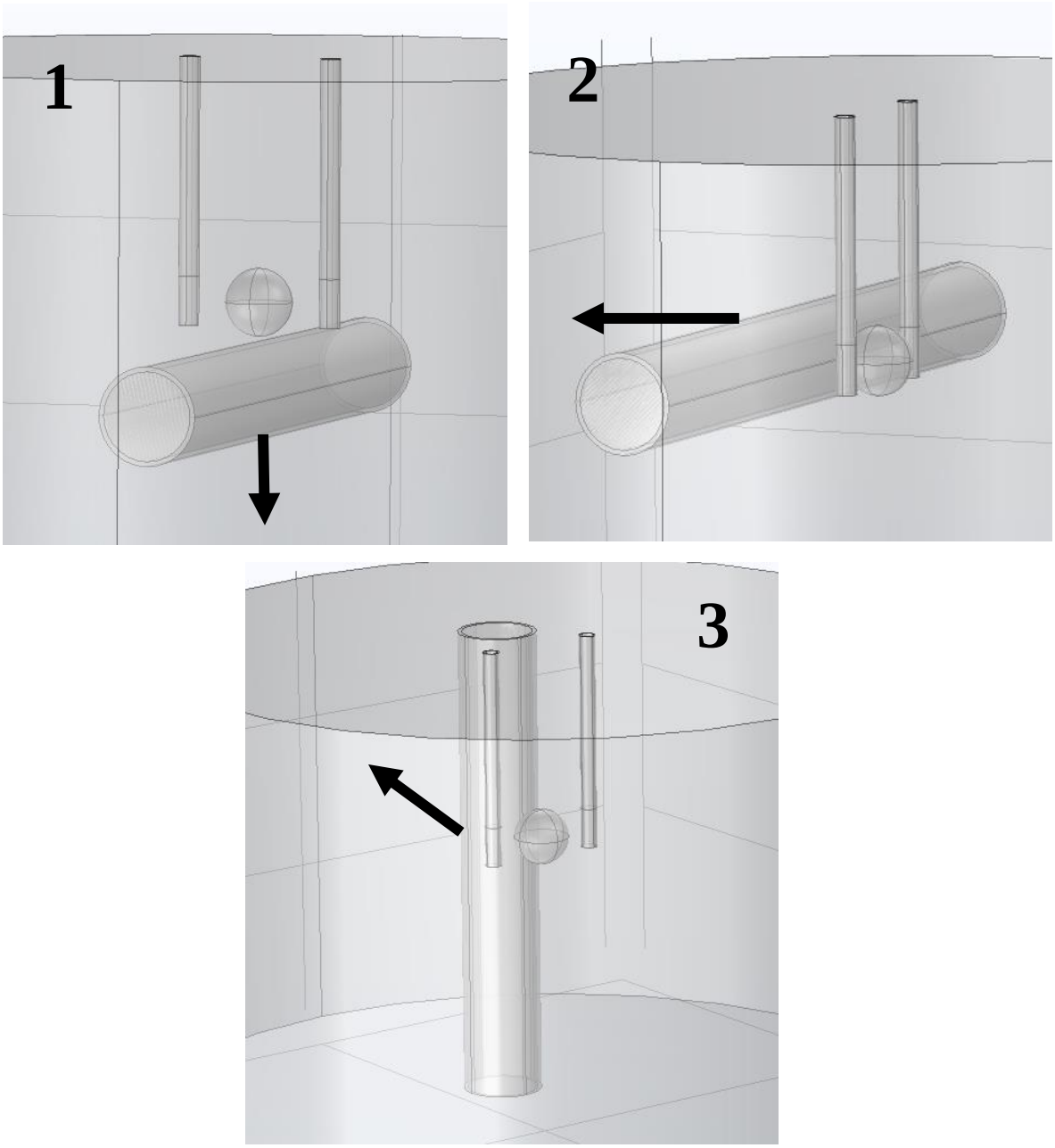

Figure 3-15: The three blood vessel configurations used in the analysis. The arrow indicates the direction that the vessel is moved away from the tumor

Each vessel is positioned as close to the tumor as possible, and then moved directly away in increments of 3 mm. The data is presented in the format of a dose volume histogram, where the y-axis represents the proportion of the volume that are above the corresponding electric field value on the x-axis. Figure 3-16, 3-17, and 3-18 presents this data for the tumor and the blood vessel wall. The electric field threshold for liver tissue death is marked on the graph [28].

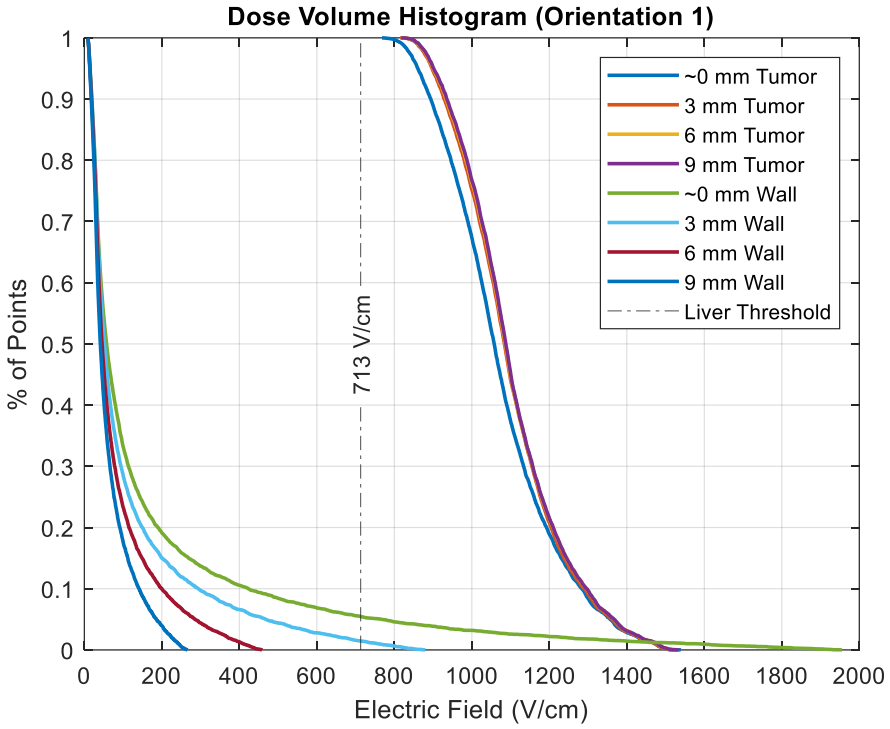

Figure 3-16: Dose volume histogram from orientation 1

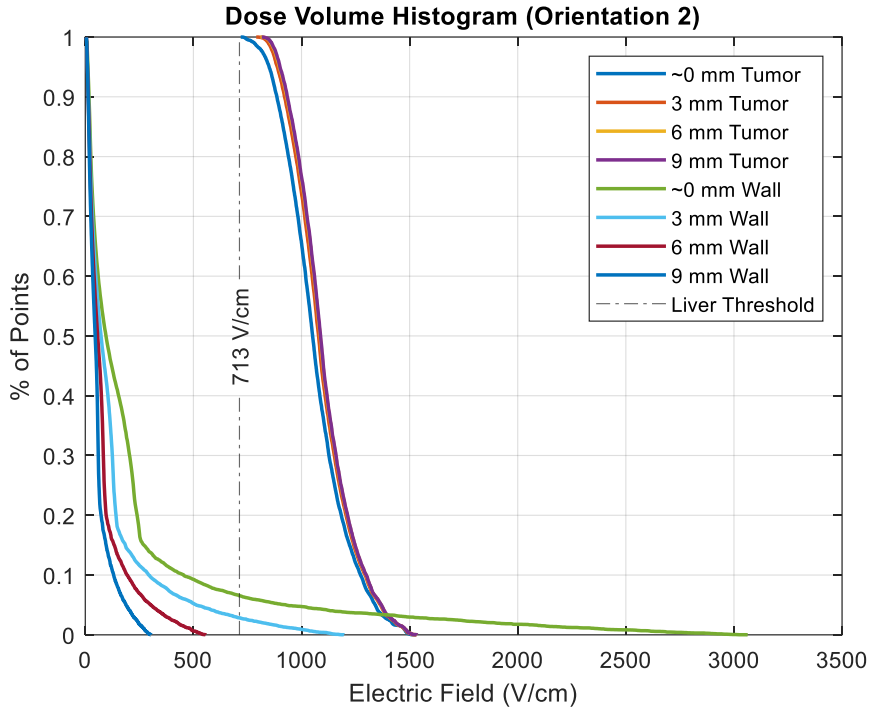

Figure 3-17: Dose volume histogram from orientation 2

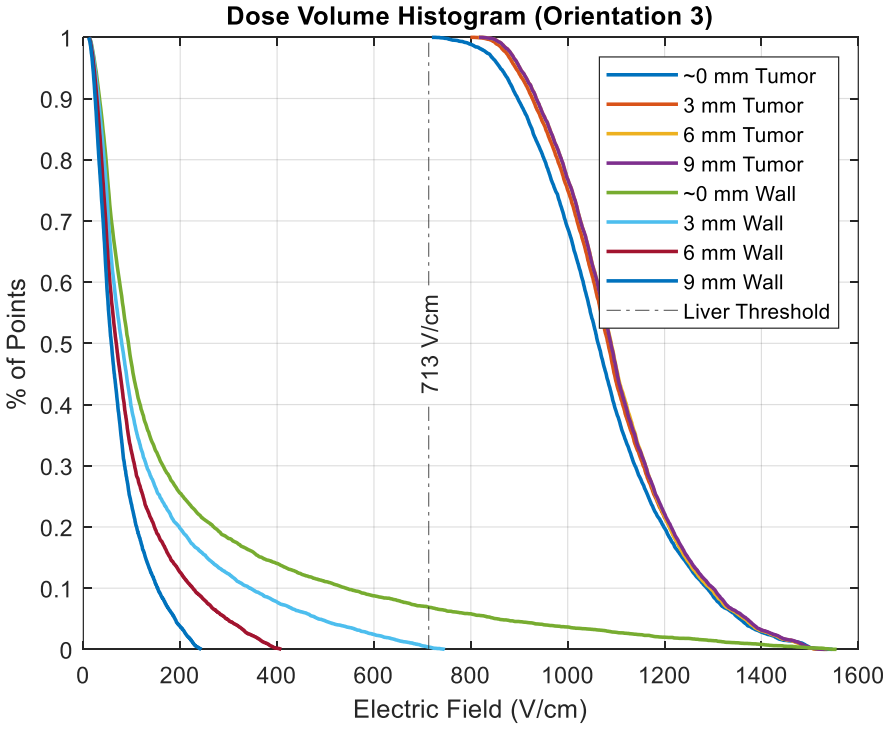

Figure 3-18: Dose volume histogram from orientation 3

IV. Discussion

The values in Table 3-3 show the optimal electric field threshold to demarcate healthy and dead tissue with the given conductivity curve. The area and DSC parameters were consistent for all of the experiments, indicating that there were no major discrepancies between total area and overall shape. Note that the conductivity curve in simulation was not changed between experiments. There could potentially be other conductivity curve shapes that would produce a better fit for the data, and more research is needed to determine this. The delay/switch time and pulse width experiments both used 100 total bursts whereas the pulse number and voltage experiments only used 10 total bursts, which is why the threshold is much lower for the high-burst experiments. An increase from 2 μs to 10 μs in the delay/switch time yielded an increase of the electric field threshold by approximately 25 V/cm, although this change is likely due to variation in tissue properties. An increase from 1 μs to 5 μs in the pulse width yielded a 75-100 V/cm decrease in the threshold. An increase in the pulse number from 25 to 75 yielded a 100 V/cm decrease in the threshold. An increase in the voltage from 1 kV to 2 kV yielded a 50 V/cm decrease in the threshold, however this change could be attributed to biological variations since the voltage was adjusted in simulation and the value should have remained constant. There were also some instances of the threshold not changing between experiments, indicating the need for repetition to verify these results.

The results from the heterogenous analysis showed that the large blood vessel has a quantifiable impact on the electric field within the tumor. The results show that there was an approximate 100 V/cm decrease in portions of the tumor that were already close to dipping below the threshold for liver cell death. Sections of the tumor that were well above the threshold saw a less pronounced change. This decrease in electric field could be the difference between recovery and recurrence since the points near the threshold are most affected by the heterogeneities. Once the vessel was more than 3 mm away from the tumor, very little change in the electric field occurs (< 10 V/cm), which indicates that heterogeneities nearly adjacent to the structure in question have the most tangible effect. The blood vessel wall also experiences a significant dose depending on the orientation, which could be problematic since the critical blood vessels must be spared. The advantage of tissue selectivity during NTIRE treatments could potentially prevent necrosis in the vessel wall, however the exact electric field threshold for this

type of tissue is currently unknown. It is worth noting that a recent study showed that applying upwards of 3800 V/cm directly to large blood vessels in rats yielded no adverse effects, so this could potentially indicate that the electric fields observed in this study are safe, however more research would be needed to confirm this for human subjects [38]. The electric field in portions of the vessel wall of orientation three reaches nearly 3000 V/cm, which could potentially cause some damage. However, the manner in which the probes are inserted into the tissue could potentially minimize the collateral damage since orientation three has a maximum field strength of around 1550 V/cm in the vessel wall. The probe setup and electric field profile for this study is not considered ideal for a realistic NTIRE treatment, however this study shows that collateral damage can be significantly minimized by optimizing the orientation of the probes relative to the critical structures.

Chapter 4 – Conclusion and Future Works

The results from this study were ultimately able to provide some new experimental data on the changes that manifest in lesions created in potato tissue when varying specific NTIRE waveform parameters. This study also demonstrated that perceptible changes occur in the electric field of treatment zones when heterogeneities such as large blood vessels are within ~3 cm. The data collection is far from complete since the data acquired in this study need trials with a greater sample size to validate any changes as statistically significant. This study was limited to experimental findings in homogenous potato tissue, and further study is warranted to assess results in tissue more representative of actual treatment sites. More heterogeneous structures should be analyzed as well, along with probe arrangements that are more representative of a real NTIRE procedure.

Once the model is refined enough to accurately predict lesions in *ex vivo* potato and liver tissue, the next step would be to compare the model results to NTIRE ablations that are performed *in vivo*. Cindrič et al. performed this analysis by acquiring 18 computed tomography data sets from human patients that received NTIRE treatment for primary and metastatic liver cancer [22].

Since irreversible electroporation is a relatively young field, there are still many questions that need to be answered before it can be fully realized as an additional tool in the tissue ablation arsenal. Ultimately, NTIRE procedures would want to move in the direction of optimized numerical treatment planning since this automated process combined with medical imaging has allowed for another method of tissue ablation, radio therapy, to become the most successful methods of treating cancer next to resection [39]. Optimization could potentially be very effective with NTIRE since the boundary established between healthy and ablated tissue is typically very sharp, therefore if the ablation region were set perfectly then very little healthy tissue would need to be damaged [40]. For such a technology to exist, there would need to be a database with as much information as possible regarding the properties of the tissue, how the tissue behaves in the presence of electric fields and temperature changes, the effects of different electrode geometries, and how the waveform shape affects cell death.

Numerically modeling electric fields and thermal changes are simple and accurate in homogenous, isotropic tissue, and would not require much optimization since there are no vital organs that need to be spared. Complex structures that vary between patients, however, would require a more in-depth knowledge of the conductivity changes to avoid damaging critical areas. The current literature on how the conductivity of tissue changes over the course of an NTIRE treatment is somewhat incomplete since there are many different combinations of waveform protocols and tissue structures that need to be tested and verified experimentally. This study attempted to avoid these experimental procedures by extrapolating data from existing literature, however performing these experiments on the tissue in question with various waveforms would yield the most accurate models and effectively expand the knowledge of NTIRE. The statistical method of characterizing cell death presented in the background section could also potentially be used for predicting lesions, however this model has received little attention in the academic community thus far.

Ideally, most of the experiments in this study would have been performed on animal tissue (bovine or porcine liver), however some complications arose during testing that made obtaining and electroporating these types of samples impractical. A perfusion model developed by Bhonsle et al. [41] could be incorporated to allow for the lesion to be contrasted from healthy tissue and to mimic the heatsinking effect of flowing liquid in the sample. The potatoes in this study have no sort of perfusion model, which would make any temperature effects seen in these experiments more pronounced than they would be in an actual treatment. Testing different probe designs would have proven useful in creating a more complete understanding of NTIRE since treatments typically involve multiple probes with varying geometries. Most of these different probe setups could be modeled accurately in Multiphysics and would not require testing to determine the resulting shape of the electric field.

References

[1] R. L. Siegel, K. D. Miller, and A. Jemal, “Cancer statistics, 2020,” *CA. Cancer J. Clin.*, vol. 70, no. 1, pp. 7–30, Jan. 2020.

[2] P. Agnass, E. van Veldhuisen, M. van Gemert, C. van der Geld, K. van Lienden, T. van Gulik, M. R. Meijerink, M. G. Besselink, H. P. Kok, and J. Crezee, “Mathematical modeling of the thermal effects of irreversible electroporation for *in vitro* , *in vivo* , and clinical use: a systematic review,” *Int. J. Hyperthermia*, vol. 37, no. 1, pp. 486–505, Jan. 2020.

[3] H.-C. Han, F. J. Ha, P. Sanders, R. Spencer, A. W. Teh, D. O'Donnell, O. Farouque, and H. S. Lim, “Atrioesophageal Fistula: Clinical Presentation, Procedural Characteristics, Diagnostic Investigations, and Treatment Outcomes,” *Circ. Arrhythm. Electrophysiol.*, vol. 10, no. 11, Nov. 2017.

[4] F. H. M. Wittkampf, “Electroporation and its Relevance for Cardiac Catheter Ablation,” *JACC Clin Electrophysiol.*, vol. 4, no. 8, p. 10, 2018.

[5] J. S. Koruth, K. Kuroki, I. Kawamura, R. Brose, R. Viswanathan, E. D. Buck, E. Donskoy, P. Neuzil, S. R. Dukkipati, and V. Y. Reddy, “Pulsed Field Ablation Versus Radiofrequency Ablation: Esophageal Injury in a Novel Porcine Model,” *Circ. Arrhythm. Electrophysiol.*, vol. 13, no. 3, Mar. 2020.

[6] M. Dollinger, F. Zeman, C. Niessen, S. A. Lang, L. P. Beyer, M. Muller, C. Stroszczynski, and P. Wiggermann, “Bile Duct Injury after Irreversible Electroporation of Hepatic Malignancies: Evaluation of MR Imaging Findings and Laboratory Values,” *J. Vasc. Interv. Radiol.*, vol. 27, no. 1, pp. 96–103, Jan. 2016.

[7] K. Pillai, J. Akhter, T. C. Chua, M. Shehata, N. Alzahrani, I. Al-Alem, and D.L. Morris, “Heat Sink Effect on Tumor Ablation Characteristics as Observed in Monopolar Radiofrequency, Bipolar Radiofrequency, and Microwave, Using Ex Vivo Calf Liver Model,” *Medicine (Baltimore).*, vol. 94, no. 9, p. 10, 2015.

[8] A. Ivorra and B. Rubinsky, “Historical Review of Irreversible Electroporation in Medicine,” in *Irreversible Electroporation*, B. Rubinsky, Ed. Berlin, Heidelberg: Springer Berlin Heidelberg, 2010, pp. 1–21.

[9] E. Neumann, M. Schaefer-Ridder, Y. Wang, and P. H. Hofschneider, “Gene transfer into mouse lyoma cells by electroporation in high electric fields.,” *EMBO J.*, vol. 1, no. 7, pp. 841–845, Jul. 1982.

[10] T. Kotnik, P. Kramar, G. Pucihar, D. Miklavcic, and M. Tarek, “Cell membrane electroporation- Part 1: The phenomenon,” *IEEE Electr. Insul. Mag.*, vol. 28, no. 5, pp. 14–23, Sep. 2012.

[11] M. L. Yarmush, A. Golberg, G. Serša, T. Kotnik, and D. Miklavčič, “Electroporation-Based Technologies for Medicine: Principles, Applications, and Challenges,” *Annu Rev Biomed Eng.*, p. 29, 2014.

[12] T. Kotnik and D. Miklavcic, “Analytical Description of Transmembrane Voltage Induced by Electric Fields on Spheroidal Cells,” *Biophys. J.*, p. 10.

[13] T. Kotnik, G. Pucihar, and D. Miklavc̆ic̆, “Induced Transmembrane Voltage and Its Correlation with Electroporation-Mediated Molecular Transport,” p. 11.

[14] P. A. Garcia, R. V. Davalos, and D. Miklavcic, “A Numerical Investigation of the Electric and Thermal Cell Kill Distributions in Electroporation-Based Therapies in Tissue,” *PLOS ONE*, vol. 9, no. 8, p. 12, 2014.
[15] A. Golberg, “A statistical model for multidimensional irreversible electroporation cell death in tissue,” *Biomed Eng Online.*, p. 9, 2010.
[16] C. B. Arena, M. B. Sano, J. H. Rossmeisl Jr., J. L. Caldwell, P. A. Garcia, M. N. Rylander, and R. V. Davalos, “High-frequency irreversible electroporation (H-FIRE) for non-thermal ablation without muscle contraction,” *Biomed. Eng. OnLine*, vol. 10, no. 1, p. 102, Dec. 2011.
[17] T. Miklovic, “A Comprehensive Characterization of Parameters Affecting High-Frequency Irreversible Electroporation Lesions,” *Ann Biomed Eng.*, p. 12.
[18] E. L. Latouche, C. B. Arena, J. W. Ivey, P. A. Garcia, T. E. Pancotto, N. Pavlisko, S. S. Verbridge, R. V. Davalos, and J. H. Rossmeisl, “High-Frequency Irreversible Electroporation for Intracranial Meningioma: A Feasibility Study in a Spontaneous Canine Tumor Model,” *Technol. Cancer Res. Treat.*, vol. 17.
[19] M. B. Sano, R. E. Fan, and L. Xing, “Asymmetric Waveforms Decrease Lethal Thresholds in High Frequency Irreversible Electroporation Therapies,” *Sci. Rep.*, vol. 7, no. 1, p. 40747, Feb. 2017.
[20] C. Bertacchini, P. M. Margotti, E. Bergamini, A. Lodi, M. Ronchetti, and R. Cadossi, “Design of an Irreversible Electroporation System for Clinical Use,” *Technol. Cancer Res. Treat.*, vol. 6, no. 4, pp. 313–320, Aug. 2007.
[21] “NanoKnife®.” https://www.pesmed.it/en/?id=products&category=nanoknife (accessed Jul. 21, 2021).
[22] H. Cindric, P. Mariappan, L. Beyer, P. Wiggermann, M. Moche, D. Miklavcic, and B. Kos, “Retrospective study for validation and improvement of numerical treatment planning of irreversible electroporation ablation for treatment of liver tumors,” *IEEE Trans. Biomed. Eng.*, pp. 1–1, 2021.
[23] R. V. Davalos, L. M. Mir, and B. Rubinsky, “Tissue Ablation with Irreversible Electroporation,” *Ann. Biomed. Eng.*, vol. 33, no. 2, pp. 223–231, Feb. 2005.
[24] A. Župani and D. Micklavcic, “Optimization and Numerical Modeling in Irreversible Electroporation Treatment Planning,” *Series in Biomed. Eng.*, p. 21.
[25] R. U. Makower, “Effect of Nucleotides on Enzymic Browning in Potato Slices,” *Plant Physiol.*, vol. 39, no. 6, pp. 956–959, Nov. 1964.
[26] S. P. Bhonsle, C. B. Arena, D. C. Sweeney, and R. V. Davalos, “Mitigation of impedance changes due to electroporation therapy using bursts of high-frequency bipolar pulses,” *Biomed. Eng. OnLine*, vol. 14, no. Suppl 3, p. S3, 2015.
[27] “DATABASE » IT’IS Foundation.” https://itis.swiss/virtual-population/tissue-properties/database/ (accessed May 25, 2021).
[28] Y. Zhao, S. Bhonsle, S. Dong, Y. Hongmei-Liu, A. Safaai-Jazi, R. V. Davalos, and C. Yao, “Characterization of Conductivity Changes During High-Frequency Irreversible Electroporation for Treatment Planning,” *IEEE Trans. Biomed. Eng.*, vol. 65, no. 8, pp. 1810–1819, Aug. 2018.
[29] J. A. Berkenbrock, G. Brasil Pintarelli, A. de Castro Antônio Júnior, and D. O. H. Suzuki, “Verification of Electroporation Models Using the Potato Tuber as In Vitro Simulation,” *J. Med. Biol. Eng.*, vol. 39, no. 2, pp. 224–229, Apr. 2019.

[30] P. Philips, D. Hays, and R. C. G. Martin, “Irreversible Electroporation Ablation (IRE) of Unresectable Soft Tissue Tumors: Learning Curve Evaluation in the First 150 Patients Treated,” *PLoS ONE*, vol. 8, no. 11, p. e76260, Nov. 2013.
[31] C. Suárez, A. Soba, F. Maglietti, N. Olaiz, and G. Marshall, “The Role of Additional Pulses in Electropermeabilization Protocols,” *PLoS ONE*, vol. 9, no. 12, p. e113413, Dec. 2014.
[32] M. Bonakdar and R. V. Davalos, “The Feasibility of a Smart Surgical Probe for Verification of IRE Treatments Using Electrical Impedance Spectroscopy,” *IEEE Trans. Biomed. Eng.*, vol. 62, no. 11, p. 11, 2015.
[33] D. Haemmerich, D. J. Schutt, A. S. Wright, J. G. Webster, and D. M. Mahvi, “Electrical conductivity measurement of excised human metastatic liver tumours before and after thermal ablation,” *Physiol. Meas.*, vol. 30, no. 5, pp. 459–466, May 2009.
[34] A. Golberg, B. G. Bruinsma, B. E. Uygun, and M. L. Yarmush, “Tissue heterogeneity in structure and conductivity contribute to cell survival during irreversible electroporation ablation by ‘electric field sinks,’” *Sci. Rep.*, vol. 5, no. 1, p. 8485, Jul. 2015.
[35] P. J. Fellows, “Heat processing,” in *Food Processing Technology*, Elsevier, 2009, pp. 339–366.
[36] A. N. Califano and A. Calvelo, “Thermal Conductivity of Potato between 50 and 100°C,” *J. Food Sci.*, vol. 56, no. 2, pp. 586–587, Mar. 1991.
[37] M. Selmi, A. A. Bin Dukhyil, and H. Belmabrouk, “Numerical Analysis of Human Cancer Therapy Using Microwave Ablation,” *Appl. Sci.*, vol. 10, no. 1, p. 211, Dec. 2019.
[38] E. Maor, A. Ivorra, J. Leor, and B. Rubinsky, “The Effect of Irreversible Electroporation on Blood Vessels,” *Technol. Cancer Res. Treat.*, vol. 6, no. 4, pp. 307–312, Aug. 2007.
[39] A. Županič and D. Miklavčič, “Optimization and Numerical Modeling in Irreversible Electroporation Treatment Planning,” in *Irreversible Electroporation*, B. Rubinsky, Ed. Berlin, Heidelberg: Springer Berlin Heidelberg, 2010, pp. 203–222.
[40] E. W. Lee, C. T. Loh, and S. T. Kee, “Imaging Guided Percutaneous Irreversible Electroporation: Ultrasound and Immunohistological Correlation,” *Technol. Cancer Res. Treat.*, vol. 6, no. 4, pp. 287–293, Aug. 2007.
[41] S. Bhonsle, M. Bonakdar, R. E. Neal, C. Aardema, J. L. Robertson, J. Howarth, H. Kavnoudias, K. R. Thomson, S. N. Goldberg, and R. V. Davalos, “Characterization of Irreversible Electroporation Ablation with a Validated Perfused Organ Model,” *J. Vasc. Interv. Radiol.*, vol. 27, no. 12, pp. 1913-1922.e2, Dec. 2016.